Aus dem Institut für Anatomie und Zellbiologie, Abteilung für Neuroanatomie

Leitung: Prof. Dr. F. Schmitz

Universitätsklinikum des Saarlandes, Homburg/Saar

High-resolution Immuno Electron Microscopic Analyses of Synaptic Ribbons in the Mouse Retina

Dissertation zur Erlangung des Grades eines Doktors der Humanmedizin

der Medizinischen Fakultät

der UNIVERSITÄT DES SAARLANDES

2025

vorgelegt von:

Stella Papadopoulos

geb. am: 10.11.1997 in Würzburg

Tag der Promotion: 12.01.2026

Dekan: Univ. Prof. Dr. M. Hannig

1. Berichterstatter: Prof. Dr. Frank Schmitz

2. Berichterstatter: Prof. Dr. Berthold Seitz

Acknowledgements

My heartfelt thanks go to my doctoral supervisor Prof. Dr. med. Frank Schmitz for generating my interest in scientific work and for the support and advice he provided me with during the preparation of the present doctoral thesis.

I also wish to thank Karin Schwarz and Shweta Suiwal for their encouragment and valuable scientific suggestions. I am especially grateful to Rene Tinschert for his endless patience in scientific discussions and explanations and his kind help throughout the preparation of my thesis work.

A huge thank you goes to Xenia Gerloff and Iason Papadopoulos for their help in the creation of the analytical software and their constant technical support and patience even after the completion of said analytical software.

I would like to thank Gabi Kiefer very much for all the advice and help with the electron microscope and for the ultrathin sections she provided and Tamara Brück for her constant support.

Many thanks to all my colleagues from the lab, who were very welcoming and with whom I had the opportunity to have interesting conversations and a wonderful time inside and outside of the lab.

Special thanks go to my parents Dr. Ruth Papadopoulos und Prof. Dr. Thomas Papadopoulos for their unconditional love and support of my academic career.

Table of Contents

Abstract

Ribbon synapses are specialized chemical synapses in vertebrates that facilitate a tonic release of neurotransmitter. The specialized organelle that is responsible for constantly providing new ready-for-release synaptic vesicles is called the synaptic ribbon and can be seen with the help of a transmission electron microscope as an electron-dense structure. It is found adjacent to the active zone (Wagner, 1997) in the presynaptic terminal of photoreceptors and bipolar cells in the retina, hair cells in the inner ear and pinealocytes in the pineal gland in the brain (Smith and Sjöstrand, 1961, Hopsu and Arstila, 1965, Matthews and Fuchs, 2010). The main protein component of synaptic ribbons is the RIBEYE scaffolding protein (Schmitz et al., 2000). RIBEYE consists of a unique N-terminal proline-rich A-Domain and a C-terminal B-Domain which is almost identical to the transcriptional regulator protein CtBP2 (Schmitz et al., 2000). RIBEYE is only expressed in ribbon synapses whereas CtBP2 is a ubiquitously expressed protein found in nearly all eukaryotic cells.

An assembly model, which was hypothesized by Schmitz et al. in 2000, suggests that the RIBEYE A-Domains build the synaptic ribbon around the core, due to their various binding sites for other RIBEYE proteins and the RIBEYE B-Domains lie on the surface of the ribbon, where they interact with NADH and multiple different proteins in the presynaptic terminal. The goal of the present study was to refine this working hypothesis by using high resolution immuno electron microscopy to analyze possible differences in distribution of the RIBEYE A- and B-Domain across the width of the synaptic ribbon in photoreceptor synapses of the mouse retina.

In order to achieve high resolution, 5 nm colloidal gold was directly conjugated to the primary antibodies, 6F4 against the RIBEYE A-Domain and 2D9 against the RIBEYE B-Domain instead of using the indirect immunogold labelling technique. Immunogold-labelled synaptic ribbons were then analyzed with a Python-based analytic software, concerning the distances of the gold particles from the midline of the synaptic ribbon in relation to the width of the ribbon. The results showed no differences in distribution between the RIBYEYE A- and B-Domain across the width of the synaptic ribbon, leading to the conclusion, that RIBEYE A-Domain and RIBEYE B-Domain are located in similar distances from the midline of the synaptic ribbon.

Zusammenfassung

Ribbon-Synapsen sind spezialisierte chemische Synapsen in Wirbeltieren, die eine tonische Freisetzung von Neurotransmittern ermöglichen. Das spezialisierte Organell, das ständig neue, freisetzungsbereite synaptische Vesikel bereitstellt, wird synaptisches Ribbon genannt. Es kann mithilfe eines Transmissionselektronenmikroskops als elektronen-dichte Struktur dargestellt werden. Es liegt in der Nähe der aktiven Zone (Wagner, 1997) im präsynaptischen Endknöpfchen von Photorezeptoren und Bipolarzellen in der Netzhaut, Haarzellen im Innenohr und Pinealozyten in der Zirbeldrüse im Gehirn (Smith und Sjöstrand, 1961, Hopsu und Arstila, 1965, Matthews und Fuchs, 2010). Der Hauptproteinbestandteil der synaptischen Ribbons ist das Gerüstprotein RIBEYE (Schmitz et al., 2000). RIBEYE besteht aus einer einzigartigen N-terminalen Prolin-reichen A-Domäne und einer C-terminalen B-Domäne, die mit dem Transkriptionsregulatorprotein CtBP2 fast identisch ist (Schmitz et al., 2000). RIBEYE wird nur in Ribbon-Synapsen exprimiert, während CtBP2 ein ubiquitär exprimiertes Protein ist, das in nahezu allen eukaryotischen Zellen vorkommt.

Ein von Schmitz et al. im Jahr 2000 vorgeschlagenes Modell zum Aufbau des Ribbons legt nahe, dass die RIBEYE A-Domänen das synaptische Ribbon um den Kern herum aufbauen, da sie über verschiedene Bindungsstellen für andere RIBEYE-Proteine verfügen, und die RIBEYE B-Domänen sich an der Oberfläche des Ribbons befinden, wo sie mit NADH und verschiedenen Proteinen im präsynaptischen Endknöpfchen interagieren. Ziel der vorliegenden Studie war es, diese Arbeitshypothese zu verfeinern, indem mittels hochauflösender Immun-Elektronenmikroskopie mögliche Unterschiede in der Verteilung der RIBEYE A- und B-Domäne über die Breite des synaptischen Ribbons in den Photorezeptorsynapsen der Mäusenetzhaut analysiert wurden.

Um eine hohe Auflösung zu erreichen, wurde kolloidales Gold mit einem Durchmesser von 5 nm direkt an die Primärantikörper, 6F4 gegen die RIBEYE A-Domäne und 2D9 gegen die RIBEYE B-Domäne, gekoppelt, anstatt die indirekte Immunogold-Markierungstechnik zu verwenden. Immunogold-markierte synaptische Ribbons wurden dann mithilfe einer Python-basierten Analysesoftware hinsichtlich der Abstände der Goldpartikel von der Mittellinie des synaptischen Ribbons in Relation zur Breite des Ribbons analysiert. Die Ergebnisse zeigten keine Unterschiede in der Verteilung zwischen der RIBEYE A- und B-Domäne über die Breite des synaptischen Ribbons. Die Schlussfolgerung ist, dass die RIBEYE A-Domäne und die RIBEYE B-Domäne in ähnlichen Abständen von der Mittellinie des synaptischen Ribbons lokalisiert sind.

1 Introduction

1.1 The Mouse Retina

The first part of the visual sensory system is the retina in the eye. The retina perceives light stimuli and transduces these light stimuli into an electrical signal. This visual sensory information passes through the neurons of the visual pathway (see below) in the retina and leaves the retina through the optic nerve. After undergoing integration in the thalamus it is processed in the visual centers in the occipital lobe of the brain and the visual association cortices in the parietal and temporal lobe.

The pars optica of the mouse retina, i.e. the light-sensitive part, is made up of several layers of cells. The general composition and structure of these layers remain the same in all mammals (Hoon et al., 2014). The outermost border of the retina is formed by the retinal pigment epithelium, which protects the retina by reducing damage from UV light and reactive oxygen species (Yang et al., 2021). Further inwards there are the first neurons of the visual pathway located, the photoreceptor cells, which convert light photons into an electrical signal. The photoreceptor cells can be divided generally into rods and cones. While the cones are responsible for photopic vision (high-acuity color vision and bright light vision), the rods execute the scotopic vision (dim-light vision), as they are 100 times more sensitive to light than the cones. In the mouse retina the rods are in the vast majority with ~ 6.4 million rods per retina and only ~ 180,000 cones per retina (Jeon et al. 1998).

The membrane disks stacked in the outer terminal of both rods and cones contain the visual pigments. In rods the visual pigment is rhodopsin and in cones there are different types of cone opsins sensitive to different wavelengths of light. Unlike the human eye, which contains three types of cones, there are only two types of cones in the mouse retina, one containing cone pigment sensitive to short wavelengths (S opsin) and the other one containing pigment sensitive to middle wavelengths (M opsin) (Hoon et al., 2014).

Rhodopsin is made up of two parts, the protein opsin and the light sensitive 11-cis-retinal that is a descendent of vitamin A. When activated by a light photon, rhodopsin is transformed into its enzymatically active form by 11-cis-retinal becoming all-trans-retinal. The active rhodopsin activates transducin, a heterotrimeric protein. GDP is bound to the inactive from of transducin. When activated by light-activated rhodopsin, the GDP is replaced by GTP and transducin dissociates into two parts, the GTP-bound alpha subunit and the beta-gamma subunits. The GTP-bound alpha subunit, aka the active transducin, activates

phosphodiesterase (PDE), an enzyme that in the active from is able to hydrolyze up to 2000 cGMP molecules per second. cGMP is responsible for sodium and calcium channels opening. Therefore, when it is hydrolyzed, the cation channels close, leading to a hyperpolarisation and decreased release of glutamate into the synaptic cleft. While cone opsin is much less sensitive to light than rhodopsin and sensitive to only specific wavelengths in the visual spectrum, the general elements of the light cascade remain the same. (Müller and Kaupp, 1998)

The outer and inner segments of both, rods and cones, make up the two outer layers of the retina. The cell bodies of the photoreceptors lie within one layer of the retina called outer nuclear layer (ONL).

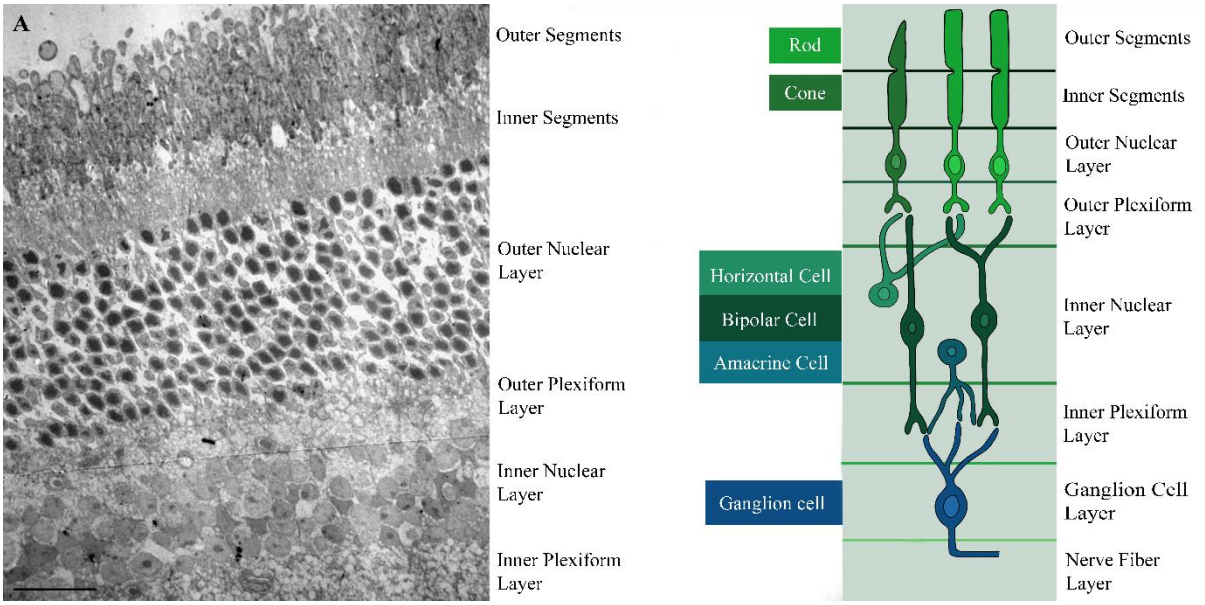

Figure 1: Layers of the Retina: A. Conventional electron microscopic image of the layers of the retina. Scale bar width shows 0.25 µm. Electron microscopic image: Laboratory resources. **B.** Schematic depiction of the neurons in the layers of the retina. Self-created for this manuscript.

In the next layer towards the inside of the eye, the outer plexiform layer (OPL), the photoreceptor cells form synapses with the rod- and cone bipolar cells. The cell bodies of the bipolar cells are located in the inner nuclear layer (INL). These second neurons can be divided into ON and OFF bipolar cells. ON bipolar cells depolarize, i.e. they become active in response to light (decreased glutamate released by photoreceptor cells). This means that the large amounts of glutamate released in the dark inhibit them via binding to mGluR6 receptors (Nakajima et al., 1993). OFF bipolar cells on the other hand hyperpolarize in response to light, and the high amounts of glutamate released in the dark causes them to become active/depolarize via binding to inotropic AMPA/kainate receptors. Cone bipolar cells can be both, ON and OFF bipolar cells, while rod bipolar cells are always ON (Silverthron et al., 2015, Masland, 2001, Ichinose and Habib, 2022). The bipolar cells form synapses with the

ganglion cells, the third neurons of the visual pathway in the inner plexiform layer (IPL). The ganglion cell axons are responsible for all sensory output of the retina towards visual centers in the brain. The cell bodies of the ganglion cells are located in the so-called ganglion cell layer. Their axons leave the retina bundled into the optic nerve.

Beside the three neurons of the visual pathway, the retina also contains interneurons and glial cells. There are two types of interneurons: horizontal cells in the outer retina interconnect photoreceptors, and amacrine cells in the inner retina connect to bipolar cells, ganglion cells and other amacrine cells. The major type of glial cells providing structural and homeostatic support to the neurons of the retina is called Müller glial cell, but astrocytes and microglia are also found in the mammalian retina (Newman and Reichenbach, 1996, Watanabe and Raff, 1988).

1.2 The Synaptic Ribbon

Synapses in the visual as well as in the auditory sensory system have special signaling requirements compared to conventional chemical synapses. These synapses have to be capable of continuous transmission for a long time, but also very fast transmission for when they receive rapidly changing stimuli. To make this possible these special synapses in the retina and inner ear of vertebrates have a specialized presynaptic organelle, called the synaptic ribbon (Wagner, 1996, Schmitz et al., 2000). The synaptic ribbon can only be found in a few types of cells in vertebrates, including the photoreceptors and the bipolar cells in the retina, but also the hair cells in the inner ear and in the cells of the pineal gland (Smith and Sjöstrand, 1961, Hopsu and Arstila, 1965, Matthews and Fuchs, 2010). For the purpose of the present study we now focused on synaptic ribbons in photoreceptor cells inside the OPL, because the synaptic ribbon is particularly large in photoreceptor synapses and thus particularly accessible for morphological analyses. The synaptic ribbon can appear in various different shapes and sizes depending on which cell type they are located in and the perspective the ribbon is shown from. In rods and cones, they are plate shaped and appear like a horse-shoe from lateral view. Under the electron microscope they mostly look bar-shaped, when they are depicted from frontal view representing the height of the ribbon, and look horse-shoe-shaped when seen from lateral view, representing the length of the ribbon (Sjöstrand et al., 1958, McCartney and Dickson 1985, Rao-Mirotznik et al., 1995, Kesharwani et al., 2021). In cones the individual ribbon is smaller than in the rods, but there are more of them, and in total they provide a larger surface area (Adly et al., 1999, Sterling and Matthews, 2005, Heidelberger et al., 2005, Thoreson, 2007, Schmitz, 2009).

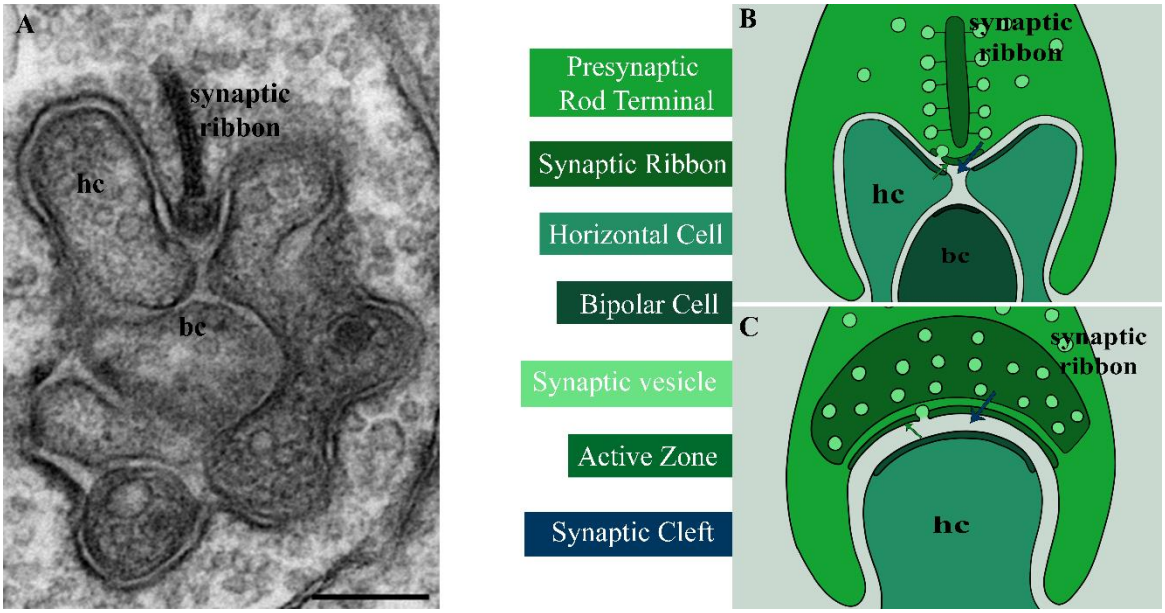

Figure 2: Synaptic Ribbon in a Rod Photoreceptor cell: A. Conventional electron microscopic image of a rod photoreceptor ribbon synapse. Abbreviations: hc = horizontal cell, bc = bipolar cell. Scale bar width shows 0.25 µm. Image: Laboratory finding **B**. Schematic depiction of the ribbon synapse of a rod photoreceptor cell from frontal view. **C.** from side view.

The synaptic ribbon works by continuously docking synaptic vesicles with the neurotransmitter glutamate and accumulating them near the active zone, supplying new vesicles for release continuously (Schmitz, 2009). When free floating vesicles inside the presynaptic terminal get close to the ribbon, they tag on to it via very fine filaments which results in synaptic vesicles being connected to the ribbon on its entire height and length (Sterling and Matthews 2005).

When triggered by influx of sodium and calcium through the cation channels, synaptic vesicles fuse with the plasma membrane. L-type voltage-gated calcium channels in photoreceptor cells of ribbon synapses are special, because they are not inactivated by calcium in the form of a negative feedback loop (Singh et at., 2006). This allows for a continuous exocytosis of synaptic vesicles in these synapses. The released vesicles are replaced quickly by ribbon-attached vesicles on a more distal site of the ribbon moving more proximally (Zenisek, 2008). A supporting mechanism for continuous glutamate release in ribbon synapses is the so-called compound fusion. Vesicles that are not directly proximal to the plasma membrane fuse with vesicles that have already released glutamate into the synaptic cleft but stay in place creating a new pathway for neurotransmitter release (Vaithianathan et al., 2016).

The second mode of neurotransmitter release made possible by synaptic ribbons beside the continuous release of vesicles is the rapid release for transmitting rapidly changing stimuli. This is made possible by nanodomains of high calcium at the distal ribbon causing rapid

exocytosis of ribbon-attached vesicles within milliseconds (Vaithianatham and Matthews, 2014)

Ribbon synapses are capable of releasing many more vesicles at once and over a much longer time span than other types of synapses without ribbons, where the synaptic vesicles are only embedded in the depressions of the active zone and deplete much quicker. In the dark the ribbon synapses in the retina are therefore able to constantly release synaptic vesicles with glutamate into the synaptic cleft. Because of the way ribbon synapses stock up on ready-for-release synaptic vesicles, they are suited to transmit a wide range of duration and intensity of a stimulus, as well as fast changes (Lagnado et al., 1996).

Because of the great ultrastructural plasticity of synaptic ribbons, ribbons of a given location and type of ribbon synapse fluctuate in size and shape. Depending on the light phase and synaptic activity, material is added and subtracted from the ribbon, resulting in longer ribbons in the dark, when the synaptic activity is increased, and shorter ribbons in the light, when the glutamate release in the ribbon synapse decreases (Balkema et al., 2001).

1.3 RIBEYE

An essential protein component making up the synaptic ribbon is a protein called RIBEYE. RIBEYE was identified by Schmitz et al. in 2000 as a major component of synaptic ribbons. RIBEYE consists of an N-terminal A-Domain and a C-terminal B-Domain. The A-Domain of RIBEYE is specific to the protein and was only found in synaptic ribbons, while the B-Domain is nearly identical to a transcriptional regulator protein called CtBP2. CtBP2 has 20 additional amino-terminal amino acids containing a nuclear localization signal. Both domains are a product of the CtBP2 gene and both are essential for building the synaptic ribbon (Maxeiner et al., 2016, Shankwar et al., 2022). A similar NADH-regulated repressor, CtBP1, which is located in the Golgi apparatus, can also be found at the synaptic ribbon, but is not needed for building a functional ribbon (Chinnadurai, 2009, tom Dieck et al., 2005). While there are many other proteins present in the ribbon synapse besides RIBEYE, they are unlikely to be responsible for the structure and function of the ribbon, because they are found also in other types of synapses without synaptic ribbons and they are not essential for the building of the synaptic ribbon.

Due to various interaction sites on the A- and B-domain that allow them to bind A- and B-Domains of other RIBEYE proteins, RIBEYE is able to self-assemble. In a study done by Magupalli et al. in 2008, cells were transfected with RIBEYE A- and B-Domain leading them

to form RIBEYE aggregates that resembled the spherical ribbons found in the hair cells of the inner ear. This prompted them to contemplate whether this spherical ribbon could be the basal type of synaptic ribbon, possibly a building unit for other forms of ribbons, like the plate-shaped synaptic ribbons of rods and cones.

Because the RIBEYE A-Domain contains multiple interaction sites for other RIBEYE A- and B-Domains, it was put forward that the A-Domain has a structural function in the ribbon (Magupalli et al., 2008). This is also consistent with the finding that deletion of the RIBEYE A-Domain leads to the disappearance of all ribbons. The B-domain contains binding region for NADH, which influences the assembly of the synaptic ribbon. Essential for this binding of NADH is a protein called Munc119 that interacts with the RIBEYE B-Domain (Alpadi et al., 2008). Several other cytosolic proteins, such as GCAP2 and ArfGAP3, also interact with the RIBEYE B-domain (Venkatesan et al., 2010, Dembla et al., 2014), suggesting that the B-Domain is located on the surface of the ribbon.

All of these findings support the working model that was proposed in 2000 by Schmitz et al. visible in Figure 3, which proposes that structural RIBEYE A-Domains build the ribbon around the core and are surrounded by B-domains lying on the surface of the ribbon and interacting with several different synaptic proteins. According to this working model, the synaptic ribbon could have a core protein that is yet unknown.

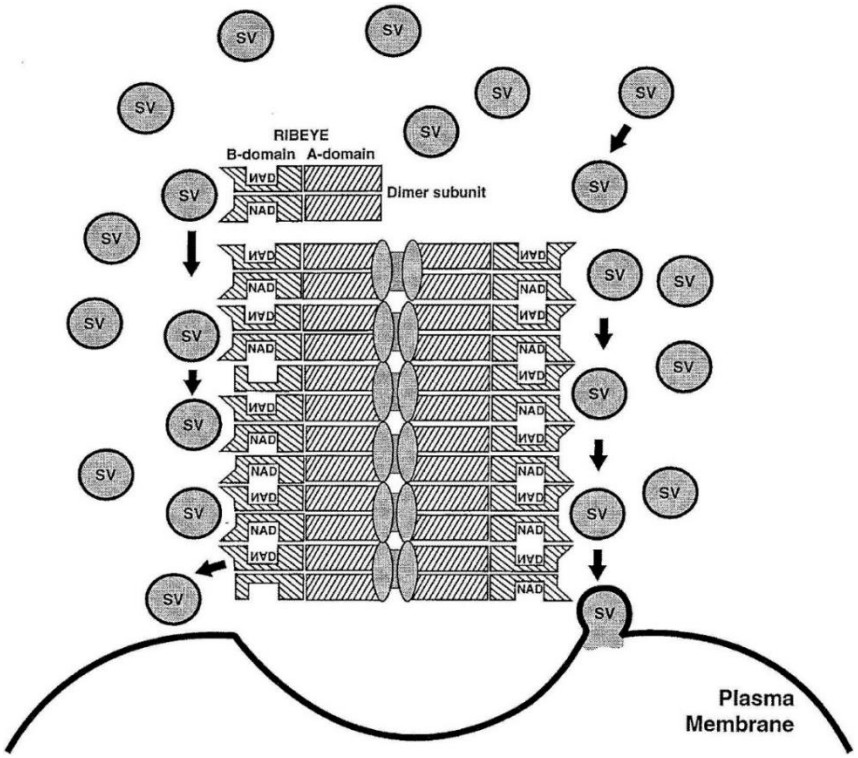

Figure 3: Working model of the structure of the synaptic ribbon proposed by Schmitz et al. in 2000: Abbreviations: SV = synaptic vesicle. Image from Schmitz et al., 2000.

1.4 Objective of the Thesis Work

While the more recent findings go along with the working hypothesis, we are far from actually knowing the structure of the synaptic ribbon. It is unknown, whether another protein is essential for the assembly of the ribbon or how many RIBEYE proteins make up the width of the ribbon. In the present study I worked to refine the assembly model by using a higher resolution electron microscopic method. In order to further reinforce the working model or disprove it, I closely looked at the distribution of RIBEYE A- and B-Domain in the synaptic ribbon of mouse photoreceptor cells. First I immunolabelled each RIBEYE domain with a specific monoclonal antibody conjugated to colloidal gold and after that I analyzed the electron microscopic images of the labelled synaptic ribbon with the help of a Python-based analytical software. The software works by calculating the relative distances of the labelled RIBEYE Domains to the midline of the ribbon in relation to the width of the ribbon. I focused on finding differences in distribution and location between the RIBEYE A- and B-Domain and compared the findings to the previous working model to obtain a refined working model.

2 Materials and Methods

2.1 Materials

2.1.1 Primary Antibodies

Anti-RIBEYE(A) 6F4: A lab-made mouse monoclonal IgG1 antibody raised against amino acids 83-211 (NP001164215) of mouse RIBEYE A-Domain (Shankwar et al., 2022), used at a dilution of 1:200 of the $(NH_4)_2SO_4$-precipitated cell culture supernatant, i.e. the antibody before Protein A affinity purification. The immunoglobulin concentration of this antibody stock was ~0.8 µg/µl, resulting in a working concentration of ~4 ng/µl. After affinity purification (resulting in stock antibody concentrations of ~0.14-0.2 µg/µl) the antibody was conjugated to 5 nm gold colloid. The gold-conjugated primary antibody was diluted 1:50 in 0.5% BSA in PBS. The final solution adjusted to final working concentrations of ~1.2-1.3 ng/µl depending on batch of affinity purification.

Anti-RIBEYE(B) 2D9: A lab-made mouse monoclonal IgG2b antibody, raised against the 12 carboxyterminal amino acids (KHGDNREHPNEQ) of mouse RIBEYE B-Domain (Dembla et al., 2018), used at a dilution of 1:200 of the non-affinity-purified $(NH_4)_2SO_4$-precipitated cell culture supernatant, which has an immunoglobulin concentration of ~0.8 µg/µl. After affinity purification (resulting in stock antibody concentrations of ~0.2-0.3 µg/µl) and conjugation to 5 nm gold colloid, the antibody was diluted 1:300 in 0.5% BSA in PBS. The final working concentrations were adjusted to ~0.22-0.25 ng/µl depending on the batch of affinity purification.

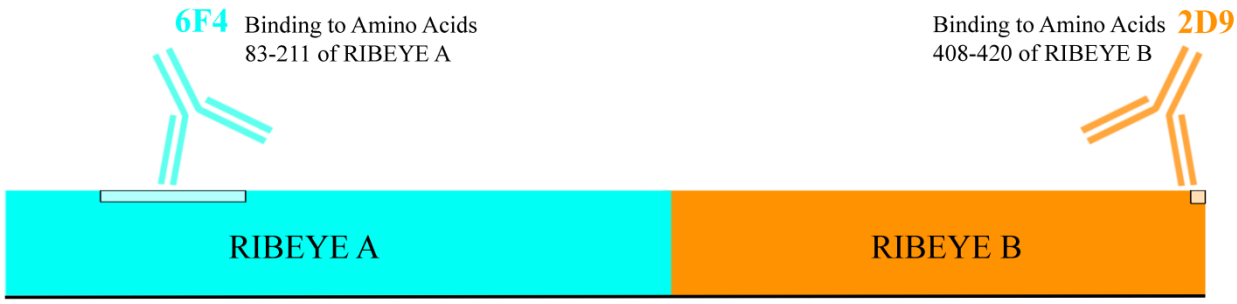

Figure 4: Schematic image of RIBEYE: The RIBEYE A-Domain is shown in turquoise, the B-Domain in orange. Mouse monoclonal antibody 6F4 is bound to the amino acids 83-211 of the A-Domain (Shankwar et al., 2022) and mouse monoclonal antibody 2D9 is bound to the 12 carboxyterminal acids of the RIBEYE B-Domain.

2.1.2 Secondary Antibodies

For post-embedding immunogold electron microscopy with the mouse monoclonal primary antibody, the secondary antibody goat anti-mouse IgG conjugated to 5 nm gold colloid (SIGMA-ALDRICH (G757)) was used. The secondary antibody was diluted 1:100 in 0.5% BSA in PBS.

2.1.3 Solutions

1x PBS	40 g NaCl 1 g KCl 7.3 g Na_2HPO_4 1.2 g KH_2PO_4 All chemicals were dissolved in H_2O and filled up to 1000 ml total volume.

Separation Gel 10%	1.5 ml dd H_2O 1.9 ml 1M Tris (pH 8.5) 2.5 ml 30% Acrylamid 75 µl 10% SDS 1.5 ml 50% Glycerol 5 µl TEMED 38 µl 10% Ammonium Persulfate (APS)
Stacking Gel	4.73 ml dd H_2O 1.88 ml 0.5M Tris (pH 6.8) 0.75 ml 30% Acrylamid 7.5 µl 10% SDS 7.5 µl TEMED 56.3 µl 10% APS
SDS Sample Buffer	1.6 g SDS 4 ml 2-Mercaptoethanol 2 ml Glycerol 2 ml 1M Tris (pH 7.0) 4 mg Bromphenolblue 2 ml H_2O
SDS-PAGE Electrophoresis Buffer	3.03 g Tris 14.4 g Glycin 1.0 g SDS
Coomassie 0.1% Staining Solution	2.5 g Brillant Coomassie Blue G250 454 ml Isopropanol 454 ml dd H_2O 92 ml Glacial Acetic Acid

Destaining Solution	50 ml Glacial Acetic Acid 100% 75 ml Ethanol 100% Filled up with H_2O to 1000 ml total volume

2.1.4 Gold Colloid

5 nm Colloidal Gold in H_2O	BBInternational (Crumlin, United Kingdom), EM.GC5

2.2 Methods

2.2.1 Processing of Mouse Retinas for Post-embedding Immunogold Electron Microscopy

The mouse retinas used in all experiments were acquired from adult C57BL/6J mice of either sex. The mice were killed in the early afternoon and the eyes were collected at environmental daylight conditions. The posterior eye-cup was dissected within 5 min post mortem, as previously described (Schmitz et al., 2000).

The posterior eye-cup with the attached retina was fixed in 2% freshly depolymerized paraformaldehyde (PFA) and 0.1% glutaraldehyde in PBS (~3 hrs, 4°C). After several washes with PBS, samples were treated with 0.1% tannic acid in PBS (1 hr, 4°C) and subsequently first washed with PBS and then with 50 mM maleate buffer (pH 5.0). Next samples were treated with 2% uranyl acetate in maleate buffer (2 hrs, 4°C). Afterwards, samples were washed with maleate buffer and H_2O and dehydrated in an ascending concentration series of pre-cooled ethanol solutions (30%, 50%, equilibrated to 4°C; 70%, 80%, 90%, 99% (2x); pre-equilibrated to -20°C; 15 min each). Samples were next infiltrated with increasing concentrations of LR Gold resin (LR-Gold/ethanol: 1:3, 1:1, 3:1 mixtures, 1 hr each at -20°C) before being transferred to pure LR Gold. LR Gold infiltration was performed overnight on an overhead rotator to promote infiltration of the LR-Gold resin. On the next day, the LR-Gold was replaced with by LR-Gold containing 0.1% benzil and samples infiltrated for ~ 2 hrs on an overhead rotator. Samples were polymerized under UV light for ~2 days at -20°C.

2.2.2 Affinity Purification using Protein A Sepharose Beads

Both RIBEYE antibodies, 6F4 and 2D9, were affinity-purified using protein A sepharose beads (SIGMA, Protein A Sepharose from Staphylococcus aureus, P3391-1), carried out as previously described by Dembla et al., 2020. This method of affinity chromatography makes use of the specific reversible binding of the Fc portion of the antibody to protein A, that is covalently coupled to the sepharose beads. This makes it possible to separate the antibody from unrelated proteins and other components of the original antibody sample.

250-500 µl of resuspended protein A sepharose beads were used for each antibody; for both antibodies, specific beads were reused for all experiments. The beads were washed four times with 1 ml of cold PBS (4°C), and then 200 µl of antibody was added to them. The beads with the antibody were incubated over night at 4°C under agitation in an overhead rotator at 3 rpm. The next day the beads with the bound antibody were sedimented by centrifuging the mixture at 4°C for 2 minutes at 13,000 rpm. The supernatant with the same unbound antibody was reused one more time in the next affinity purification. The beads were washed four times with 1 ml of cold PBS. To separate the bound antibody from the beads, 200 µl of 0.2 M glycine (pH 2.7) was added and incubated at 4°C for 5 minutes in the overhead rotator at 3 rpm. To collect the affinity-purified antibody, the beads were centrifuged for 1 minute at 4°C and 13,000 rpm. The supernatant with the purified antibody was carefully removed. 9 µl of 1M Tris (pH 8.5) was added to the purified antibody to neutralize the pH to a pH of 7.4.

To quantify the concentration of purified antibody, Thermo Fisher´s NanoDrop One Spectrophometer was used. The device measures absorbance at a wavelength of 260 nm and 280 nm and the absorbance ratio (A260/A280), therefore being able to quantify purified protein containing amino acids like tryptophan or tyrosine as well as Cys-Cys disulfide bonds (Edelhoch, 1967). The measured concentration of protein content in the affinity-purified antibody sample, was compared to the original non-purified antibody sample. The affinity-purified antibody was stored at -20°C until further use.

2.2.3 SDS-PAGE

To determine the protein content of both purified antibody samples, 6F4 and 2D9, and to verify the effectiveness of the purification, SDS-PAGE was performed as previously described (Schmitz et al., 2000). This method of discontinuous electrophoresis developed by Ulrich K. Laemmli allows the separation of proteins purely by mass, not by charge, by loading the proteins with sodium dodecyl sulfate (SDS) to completely cover the proteins‘ own charge (Laemmli, 1970).

For SDS-PAGE 5 µg of the purified antibody was dissolved in 5 µl of Laemmli sample buffer and heated up at 96°C for 10 minutes to break up the secondary and tertiary structure of the proteins. The 10% separation gel was loaded between two glass plates in a vertical electrophoresis unit and the stacking gel was poured on top of the polymerized separation gel. After the polymerization of the stacking gel the electrophoresis unit was inserted into the electrophoresis chamber and the samples were filled into the respective loading wells, as well as one well with 5 µl of protein marker (Roti-Mark STANDARD, Carl Roth GmbH, 2242.2). In the electrophoresis chamber the gel is placed between cathode and anode and electrically connected to the surrounding SDS-PAGE electrophoresis buffer. This allows the protein to be separated by molecular mass as it moves toward the anode in the separation gel. After the dye front had reached the lower end of the separation gel, the gel was removed from the electrophoresis chamber and the unit, and placed in the Coomassie Staining Solution for approximately 1 hr with gentle agitation. Afterwards, the gel was placed in the destaining solution until the protein bands could be discriminated from the background and become well visible.

The non-affinity-purified antibody samples were used as a reference in SDS-PAGE.

2.2.4 Transmission Electron Microscopy

The Tecnai 12 BioTwin Transmission Electron Microscope (FEI, Einthoven, Netherlands) was used to analyse the immunogold-labelled ultra-thin sections and to visualize the binding of the RIBEYE antibodies to the ribbon. The images were acquired with the help of the iTEM acquisition Software (Olympus, Hamburg, Germany) with a Megaview III digital camera (Gaten, Unterschleissheim, Germany). All images taken show synaptic ribbons of photoreceptor cells in the outer plexiform layer (OPL) of the mouse retina at a 135,000x magnification. Synaptic ribbons were chosen regardless of their orientation in the section. Both front and lateral view, depicting height and length of the ribbon respectively, have been used for analysis in the experiment.

Direct conjugation of affinity-purified antibodies to 5 nm gold colloid

To remove the glycine after the affinity purification, the antibodies were dialyzed overnight at 4°C against 1 L of 2 mM borate buffer (pH 9.0) using Snake Skin Dialysis Tubings (10K MWCO, 35 mm dry I.D. Thermo Scientific, Rockford, USA). Before the dialysis the dialysis membrane was previously hydrated by boiling in H_2O. After dialysis 5 µg of 6F4 in a volume of 20-36 µl and 5 µg of 2D9 in a volume of 16-27 µl were each added to 50 µl of 5 nm gold colloid (BBInternational gold colloid 5 nm in H_2O, EM.GC5) and incubated for 1 hr, allowing

the adsorption of the antibody on the colloidal gold. Colloidal gold can be very effective used this way as a marker because its special adsorption properties allow it to bind to various different proteins with very different characteristics (Faulk and Taylor, 1971). Also the high contrast and homogenous size and shape make it a very well visible under the transmission electron microscope. The secondary antibody, labelled with colloidal gold, which was used for the positive control (see below), makes use of these same properties. This way of proteins being adsorbed on colloidal gold was already described (Slot and Geuze, 1985; Horrisberger and Clerc, 1985) and remains one of the most widely used immunocytochemical methods.

The conjugated antibodies were stored at 4 °C under constant agitation in an overhead rotator to avoid clustering of the colloid gold.

Post-embedding Immunogold Labelling

Post-embedding immunogold labelling was performed with the RIBEYE antibodies directly conjugated to gold, without any secondary antibody, while the labelling of the positive control was carried out with the indirect immunogold labelling method as previously described (Schmitz et al., 2000), using the standard indirect method with the corresponding secondary antibody conjugated to gold. Ultra-thin sections with a thickness of 50-70 nm of wild-type C57BL/6J mouse retina were used.

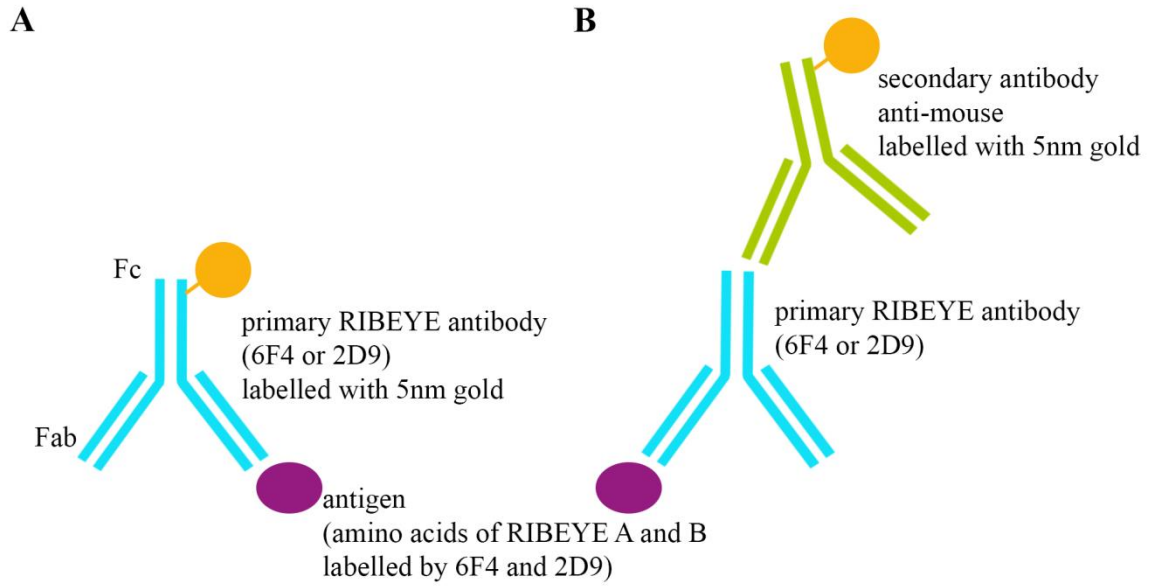

Figure 5: Direct and indirect method of immunogold labelling: A. The primary antibody was used as the only antibody, directly conjugated to 5 nm gold colloid, decreasing the distance between the gold particles and the antigen it is labelling. **B**. The primary antibody is labelled indirectly with the help of the secondary antibody. The secondary antibody is conjugated to 5 nm gold colloid.

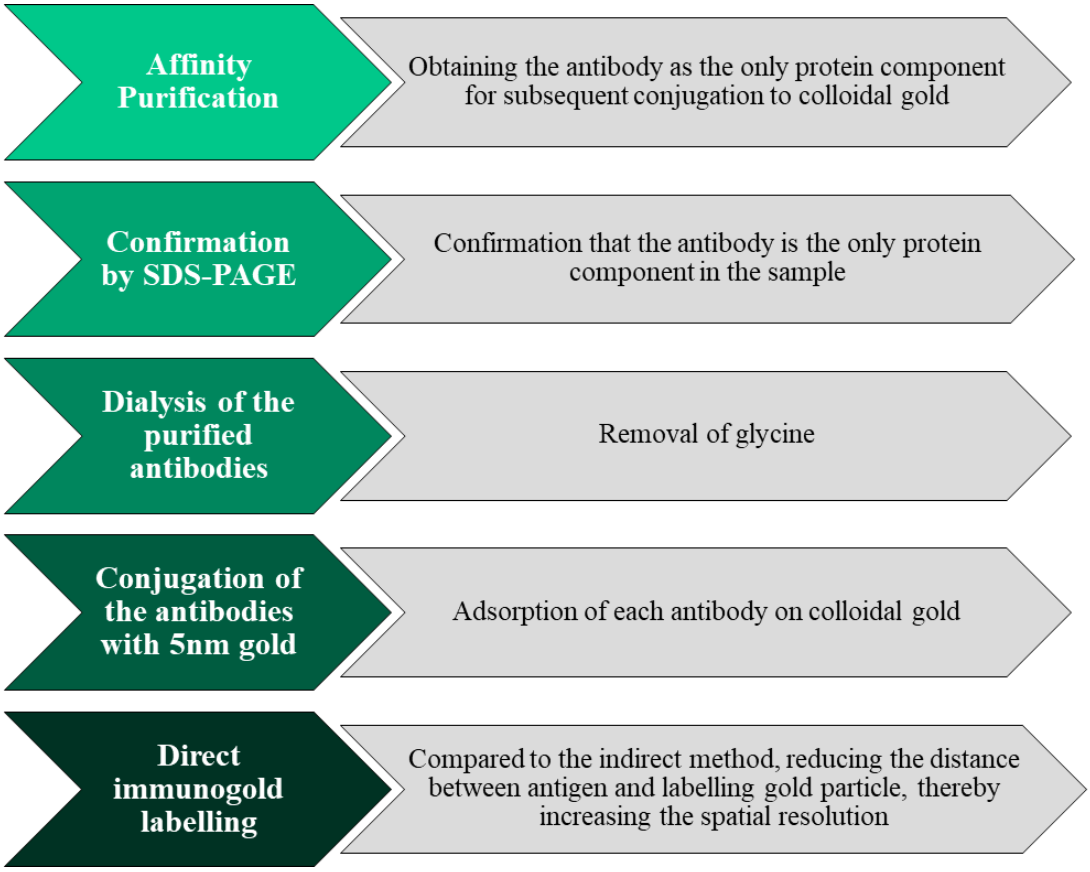

Figure 6: Steps taken for the direct method of immunogold labelling.

Initially, six immunogold labelled grids with sections from one wild-type mouse retina were prepared for the experiment, three grids immunogold labelled with 6F4 and three with 2D9. To verify the results, two more wild-type mouse retinas were prepared. For each of these mice one grid labelled with 6F4 and one grid labelled with 2D9 were used for analysis.

First the sections were incubated in 0.5 % bovine serum albumin (BSA in PBS) for 45 minutes to block unspecific binding. After that, they were incubated in the primary antibody dilution overnight at 4 °C. As the primary antibody, 6F4 and 2D9 in their affinity-purified form conjugated to 5 nm gold colloid were used (6F4 at a dilution of 1:50 in 0.5 % BSA, 2D9 at a dilution of 1:300 in 0.5 % BSA). After washing with PBS several times, the sections were fixed with 2.5 % glutaraldehyde in PBS for 15 minutes and washed with PBS again. Next they were washed with H_2O several times, before being contrasted with 2 % uranyl acetate in H_2O for 15 minutes. Finally the sections were washed again in H_2O and air dried.

As a positive control, both 6F4 and 2D9 were used in their non-affinity-purified and affinity-purified form, labelled with the gold-conjugated secondary antibody (indirect method of immunogold labelling). The dilutions of the purified 6F4 and 2D9 were adjusted to have equivalent concentrations to their non-affinity-purified forms according to the concentration determined by NanoDrop. The secondary antibody goat anti-mouse IgG 5 nm colloid gold

was incubated for 1 hr at the dilution of 1:100 in 0.5 % BSA after the incubation of the primary antibody. The grids were washed with PBS before and after the incubation of the secondary antibody. For the negative control sections were prepared using colloidal gold diluted 1:100 in 0.5% BSA instead of a primary antibody, incubating the section over night at 4 °C. No secondary antibody was used on the negative control. The specificity of both RIBEYE antibodies, 6F4 and 2D9, has also previously been verified by control experiments on RIBEYE knockout mice (Dembla et al., 2018, Shankwar et al., 2022).

2.2.5 Topographical Analysis of Ribbon-bound Gold Particles in the Transmission Electron Microscopy Images

The images taken with the transmission electron microscope were analyzed by using a custom analytical software (see below), assigning each ribbon-bound gold particle a relative distance from the midline of the ribbon in relation to the width of the ribbon. The software was newly created in Python for this purpose in the present study.

The images taken of every grid were kept separate for the analysis. For the first mouse this resulted in six groups of images; three from the three grids labelled with gold-conjugated 6F4 monoclonal antibody against RIBEYE A-Domain and three groups of images from the three grids labelled with gold-conjugated 2D9 monoclonal antibody against RIBEYE B-Domain. For mouse 2 and 3 there are additionally two groups of images each, one from the grid labelled with gold-conjugated 6F4 and one from the grid labelled with gold-conjugated 2D9. The experiment was blinded before taking the images to eliminate experimental biases during the analysis.

In preparation for the analysis by the software, the images were prepared using Adobe Photoshop CS6 (Adobe Systems Incorporated). The electron-dense area of the ribbon was marked manually, especially paying attention to exclude any visible synaptic vesicles from the area of the ribbon. The marked area was then surrounded with a line by Photoshop, marking the outer border of the ribbon. A digital ruler was used in Photoshop to mark 5-20 midpoints between the borders of the ribbon along its whole length, the amount depending on size and curvature of the synaptic ribbon. The midpoints were connected to form the midline of the ribbon. Each ribbon-bound gold particle was marked. In order to enable the software to distinguish them, the particles inside the area of the ribbon were marked in one colour, the gold particles lying outside the marked area were marked in another colour (see Figure 7). Of course it has to be pointed out that the particles lying outside of the marked areas of the ribbon are still bound to the surface of the ribbon and none of the gold is actually bound

outside of the synaptic ribbon, but due to the nature of marking the ribbons in the most exact way and the function of the analyzing software (see below) there has to be a made distinction between the particles inside and outside of the marked area.

The processed images were run through the Python-based analytical software, which analyzed the coordinates of the outer border, the midline, and the marked gold particles. Thereby, it established for each marked gold particle the **distance 1 (d1)**, the minimal distance from the midline to the gold particle, and the **distance 2 (d2)**, the minimal distance from the gold particle to the outer border of the ribbon. For each marked gold particle located inside the area of the ribbon the relative distance to the midline in relation to the width of the ribbon (d_i) was calculated by using the following formula:

$$d_i = \frac{d1}{d1 + d2}$$

d1 = minimal distance from the midline to the gold particle

d2 = minimal distance from the gold particle to the outer border of the ribbon

For calculating the relative distance of each marked gold particle outside of the area of the ribbon (d_o) the following formula was used:

$$d_o = \frac{d1}{d1 - d2}$$

d1 = minimal distance from the midline to the gold particle

d2 = minimal distance from the gold particle to the outer border of the ribbon

These two formulas allow the software to assign each gold particle inside the area of the ribbon a relative distance (d_i) from zero to one, zero being located on the midline of the ribbon, one being located on the outer border, and each gold particle outside the area of the ribbon a relative distance (d_o) >1.

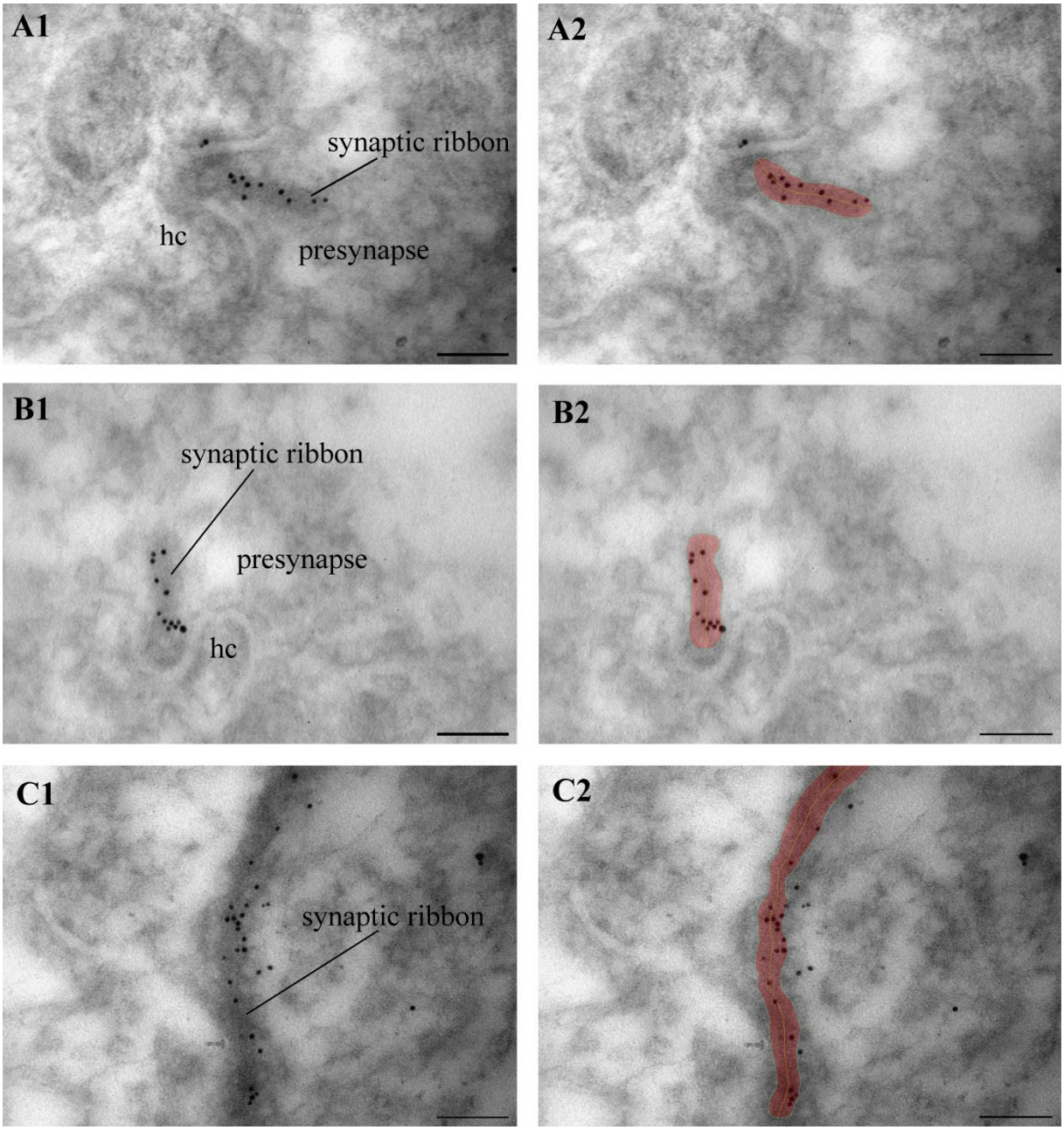

Figure 7: Preparation of the image for the analysis by the software: The following structures were marked: the area of the ribbon (red), the surrounding border (turquois), the midline through the length of the ribbon (yellow), the gold particles inside the red area (dark blue), and the particles outside the red area (light green). Abbreviations: hc = horizontal cell. Scale bar: 100 nm. Papadopoulos et al., 2024.

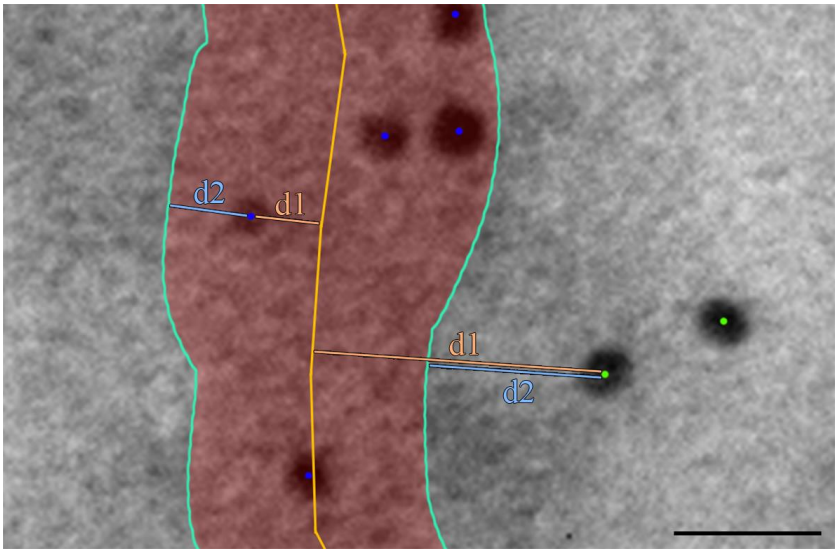

Particles inside the red area

$$d_i = \frac{d1}{d1+d2}$$

Particles outside of the red area

$$d_o = \frac{d1}{d1-d2}$$

d1 = minimal distance from the midline to the gold particle

d2 = minimal distance from the gold particle to the outer border of the ribbon

Figure 8: Analysis of every marked gold particle by the software: Distances d1 (orange) and d2 (blue) shown exemplarily for one marked gold particle inside (dark blue) and one outside (light green) the red area. Scale bar: 20 nm. Figure modified from Papadopoulos et al., 2024.

The software provides all relative distances measured. The closer to zero the relative distance, the closer the gold particles are to the middle of the ribbon, as well as the number of gold particles, analyzed inside and outside the area of the ribbon for every picture. The relative distances of each antibody for each of the mice were plotted in a histogram, depicting the amount of gold particles for each relative distance (d_{rel}), the relative distances from zero to one (d_i) representing the gold particles inside the area of the ribbon and distances above one (d_o) representing the gold particles outside.

2.2.6 Statistical Analysis

The statistical analysis of the data acquired by the analysis of the TEM pictures by the software was done with the help of the software OriginPro 2018b (OriginLab Corporation 1991-2018) and Prism (GraphPad Software, Boston, USA).

First outliers in the relative distances were identified in a box plot of each of the grids. Outliers were confirmed with the non-parametric Walsh Test and excluded from the experiment.

To depict the results in a clearer way and compare the histograms of each antibody to each other, a logistic graph was fitted to all histograms, using the following function:

$$f: [0, 13] \rightarrow R,\ x \mapsto f(d_{rel}) = a_2 + \frac{(a_1 - a_2)}{1 + \left(\frac{d_{rel}}{d_{rel\ center}}\right)^p}$$

$a_1 = f(d_{rel}=0)$

$a_2 = \lim_{d_{rel} \rightarrow \infty} f(d_{rel})$

p = power

The logistic fits of both antibodies were compared by normalizing each value to $f(d_{rel} = 0)$ (the number of gold particles analyzed at the relative distance of zero, i.e. on the midline of all ribbons immunogold labelled with one antibody) and overlaying the graphs on each other. Additionally, the rate of change of the number of particles with the relative distance (first derivative $\frac{d}{dd_{rel}}$(Au-particles/ribbon)) was analyzed and plotted, to visualize the changes in the two graphs.

"For each antibody and each of its grids, the number of gold particles per ribbon in the interval d_i was compared to the number of gold particles per ribbon in the interval d_o, and the antibodies were then compared to each other, using the non-parametric Kruskal-Wallis test, followed by a post hoc Dunn´s test. The results were depicted in a box plot, showing the differences between the number of gold particles inside and outside the area of the ribbon. Also, the percentage of the number of particles inside (d_i) and outside (d_o) of the marked area compared to the number of all gold particles was calculated for each antibody and compared"[27] using the Kruskal-Wallis followed by post hoc Dunn´s test. Finally those results were also depicted as a box plot."

3 Results

In the present study the location and distribution of RIBEYE A- and B-Domain on the synaptic ribbon was analyzed with the help of the RIBEYE antibodies 6F4 (against the A-Domain of RIBEYE) and 2D9 (against the B-Domain of RIBEYE). To accurately analyse this, first the spatial resolution was increased by direct method of immunogold labelling, then images of the immunogold labelled ribbons were acquired with the transmission electron microscope, and finally these images were analysed regarding the distribution of gold particles.

3.1 Purification of the 6F4 and 2D9 Monoclonal Antibodies for Conjugation with Colloidal Gold

The accuracy of the results of immunogold labelling was increased by using the method of direct immunogold labelling. In contrast to the indirect method which uses two antibodies to mark the antigen with the gold particle, the direct method only uses a single antibody labelled with colloidal gold, therefore decreasing the distance between gold particle and antigen and increasing the spatial resolution.

The colloidal gold is able to bind to numerous different proteins, therefore all other proteins (such as for example albumin) needed to be removed from the antibody, to prevent them from binding to the colloid gold instead of the antibody. Therefore, affinity purification was performed to remove non-immunogold components. The affinity purification with Protein A Sepharose resulted in purified antibody samples that only contained the antibody, as judged by SDS-PAGE. SDS-PAGE demonstrated that only the heavy and light chain of the antibody were present in the affinity-purified antibody solution (Figure 9). The affinity purified antibody sample of both RIBEYE antibodies, 6F4 and 2D9, showed only two protein bands, one at ~50 kDa representing the heavy chains of the antibodies and one at ~ 23.5 kDa representing the light chains of the antibodies. The non-purified antibody samples of 6F4 and 2D9 on the other hand had each additionally another band at ~ 66.5 kDa as well as other bands representing proteins that have been removed by affinity purification, such as albumin.

The protein concentration of the affinity purified antibody was measured at a wavelength of 280nm with the NanoDrop One Spectrophometer. As expected, the purified antibody showed consistently lower concentrations of protein at this wavelength than the original non-purified sample. The affinity purified 6F4 typically had A280 protein concentrations of ~0.14-0.2

µg/µl, compared to the protein concentration of ~0.8 µg/µl of the non-purified 6F4. The affinity purified 2D9 typically displayed A280 protein concentrations of ~0.2-0.3 µg/µl, while the non-purified antibody sample had A280 protein concentrations of ~0.8 µg/µl.

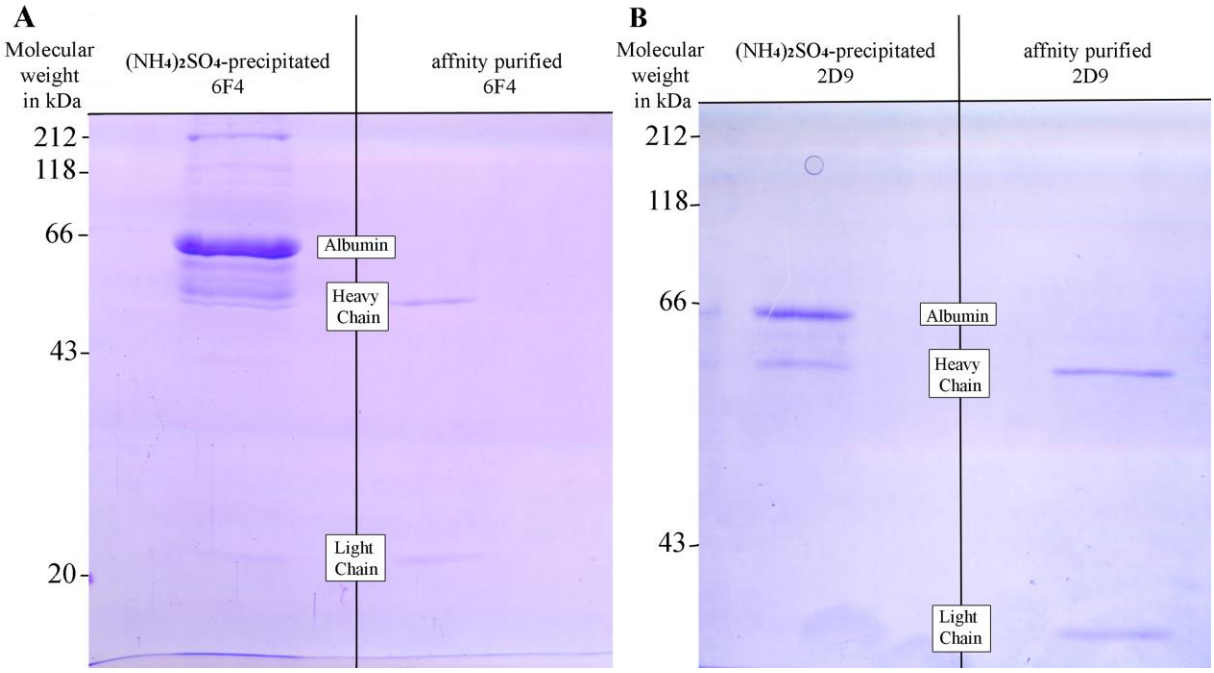

Figure 9: Protein bands of 6F4 (A) and 2D9 (B) samples before and after affinity purification: While both of the non-affinity purified antibody samples show several protein bands, the affinity purified antibodies display only 2 protein bands, representing the heavy and the light chains of both antibodies respectively.

The antibodies were used for immunogold labelling before and after affinity purification and images were taken in the transmission electron microscope, ensuring proper function of both purified antibodies and comparing the quality of immunogold labelling before and after affinity purification. As is visible in Figure 10 the results of immunogold labelling look very similar before and after affinity purification for both, 6F4 and 2D9. The affinity purification did not decrease the labelling density and labelling specificity or function of either antibody.

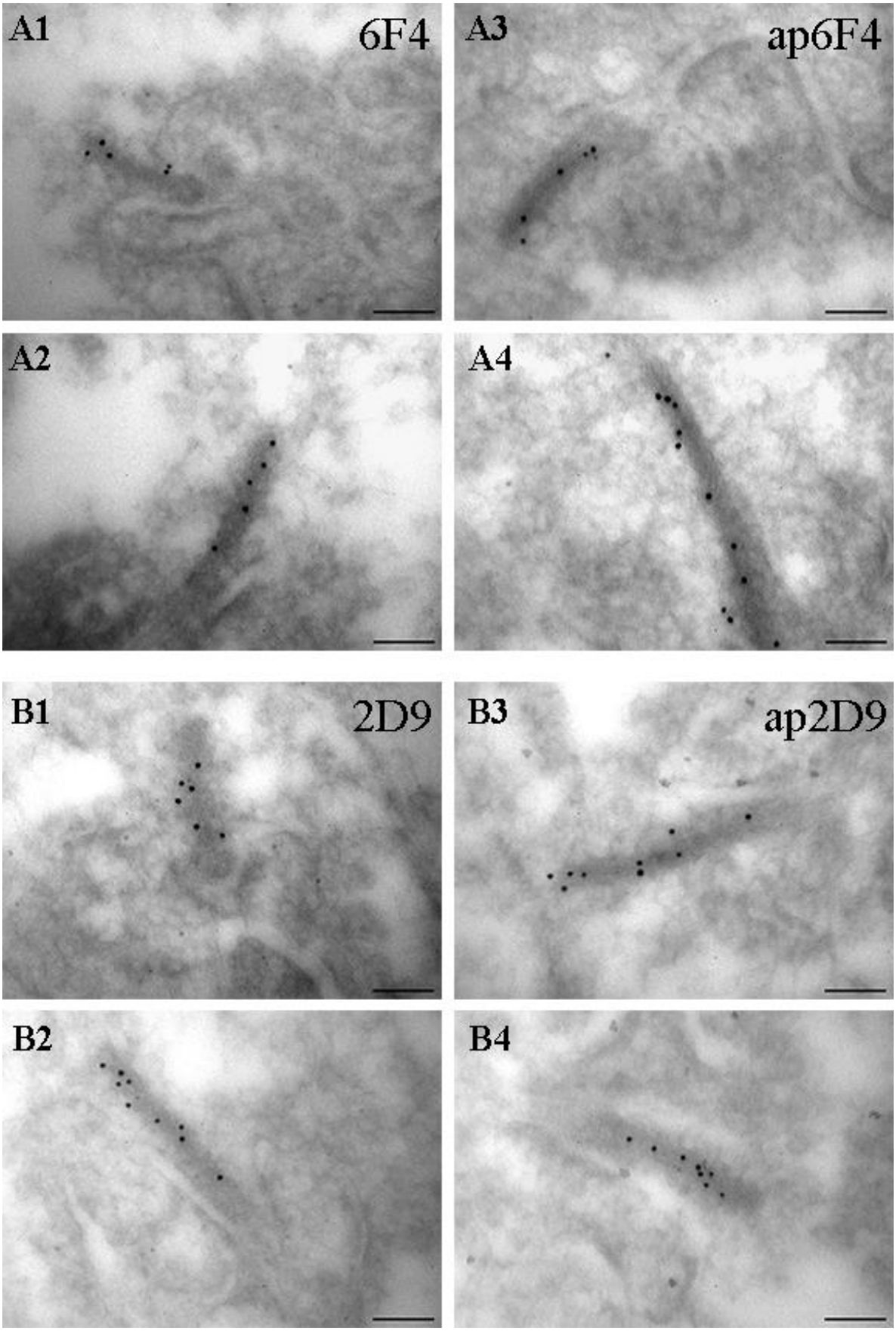

Figure 10: Comparison of 6F4 before (A1-A2) and after (A3-A4) affinity purification and comparison of 2D9 before (B1-B2) and after (B3-B4) affinity purification: Abbreviations: ap6F4 = affinity purified 6F4, ap2D9 = affinity purified 2D9. Scale bar: 100 nm.

3.2 Transmission Electron Microscopy

Next, both RIBEYE antibodies, 6F4 and 2D9, were conjugated to 5 nm gold colloid and tested again by immunogold labelling. Even though it is visible that 2D9 has a stronger affinity to RIBEYE B and has therefore more bound gold particles per ribbon than 6F4 has to RIBEYE A, at this point there was no trend in visible differences in distribution of the gold particles on the synaptic ribbon between grids labelled with 6F4, showing the A-Domain of RIBEYE, and grids labelled with 2D9, showing the B-Domain of RIBEYE.

The negative control shows no gold bound to the synaptic ribbons. This proves that the 5nm colloidal gold, which was used for conjugation with both 6F4 and 2D9, is not able to bind to the synaptic ribbon by itself. This confirms that the gold bound to the synaptic ribbon in the final experiment is the gold marking the two antibodies, 6F4 and 2D9, it is conjugated to.

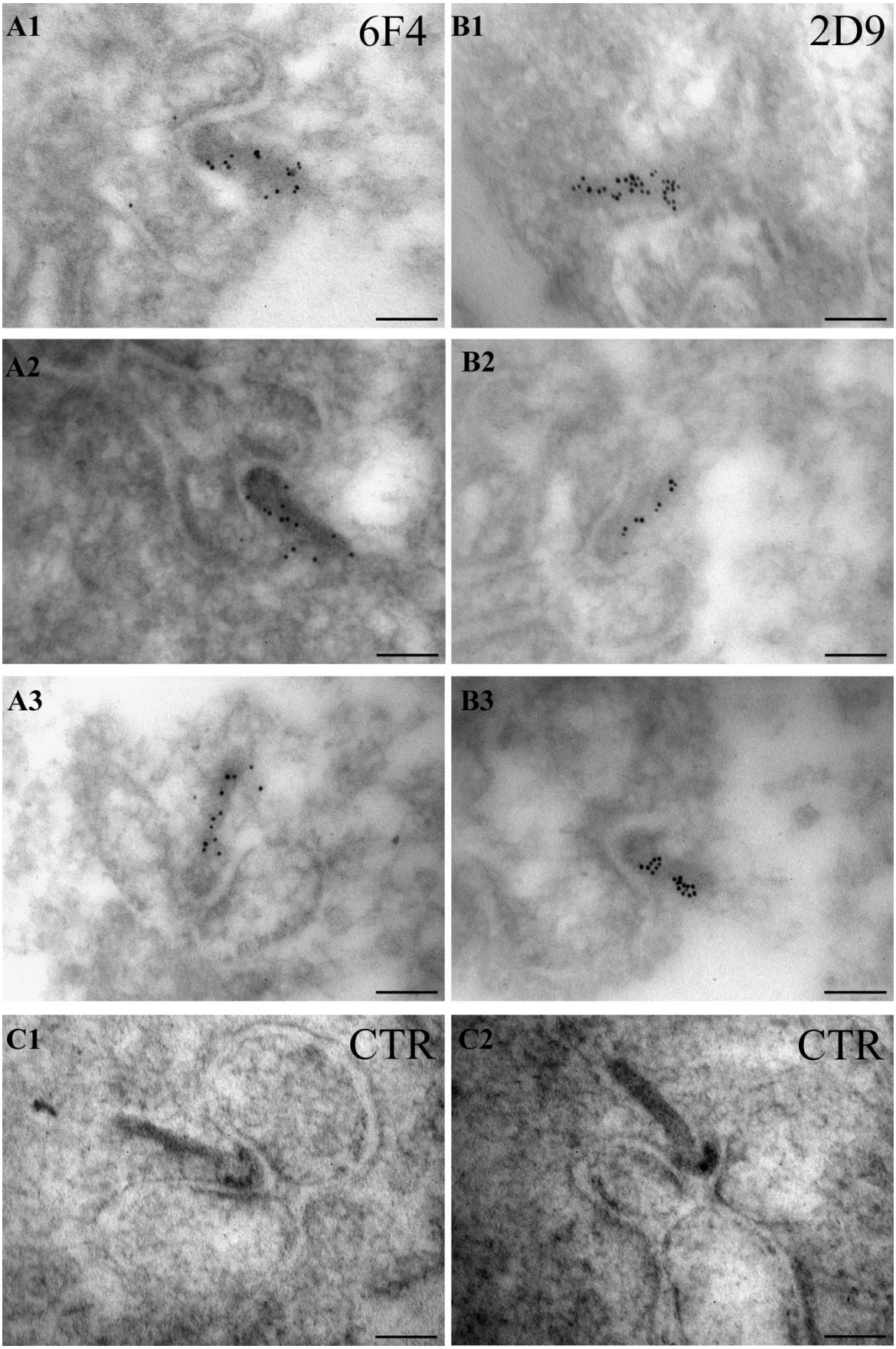

Figure 11: Direct method of postembedding immunogold labelling with 6F4 directly conjugated to 5 nm gold colloid (A1-A3) and 2D9 directly conjugated to 5 nm gold colloid (B1-B3). Images C1-C2 show the ribbons in the negative control (CTR): No trends in distribution of the gold particle are visible. Scale bar: 100 nm.

3.3 Topographical Analysis

After the blinded acquisition of the electron microscope images, the topographical analysis of the images was carried out by the Python-based analytical software. The results showed the relative distances of every single gold particle, bound to the synaptic ribbon, to the midline of the ribbon in relation to the width of the ribbon. The relative distance of zero represents gold particles lying on the midline of the ribbon; the relative distance of one represents gold particles lying on the outer border of the ribbon. Every gold particle with a relative distance above one lies outside the outer borders of the ribbon and is bound to its surface.

The relative distances of the gold particles of each grid were combined to plot a histogram. The histograms show the number of gold particles located at each relative distance. For the first mouse (m1) there are three grids labelled with 6F4 and three grids labelled with 2D9. The relative distances from each of those grids are separately shown in histograms (Figure 12). In Figure 13 all relative distances of the three grids labelled with 6F4 were combined into one histogram, showing the number of all gold particles labelling the A-Domain of RIBEYE at a given relative distances to the midline. The same was done with all relative distances of the 2D9 labelled grids of m1, resulting in one histogram, showing the relative distances of all gold particles labelling the RIBEYE B-Domain. For mouse 2 and 3 (m2 & m3) there are two histograms each, one showing the results of the 6F4-labelled grid and the other showing the results from the 2D9-labelled grid.

In every histogram of either antibody it is apparent that the largest amount of gold particles lies within the marked borders of the ribbon. This was also confirmed later in the statistical analysis (see below). Within the borders of the ribbon, the number of gold particles decreases towards the outer border of the ribbon equally in all grids of both antibodies. This trend continues outside of the borders of the ribbon for the amount of gold particles bound to the surface of the ribbon, which generally decreases the further away the gold is located from the midline. The distribution of gold particles doesn't vary visibly, neither between the individual mice in the grids labelled with the same antibody nor between the two antibodies 6F4 and 2D9. No tendencies are visible, suggesting that the A- and B-Domain of RIBEYE are distributed equally across the width of the ribbon.

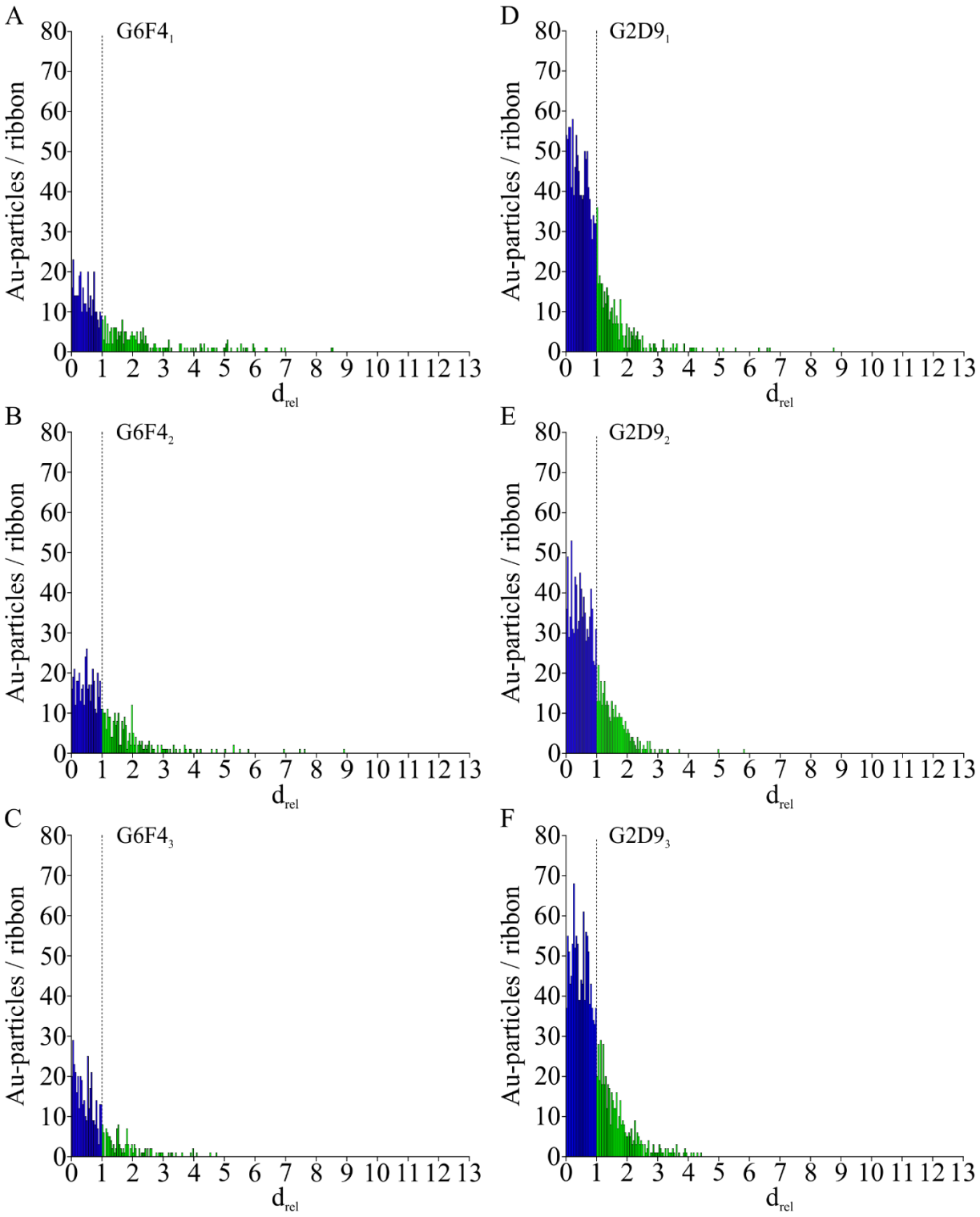

Figure 12: Histograms of Mouse 1 (m1), the 3 grids labelled with 6F4 (A-C) and the 3 grids labelled with 2D9 (D-F), showing the number of gold particles for each relative distance: The relative distances from 0 to 1 (d_i) represent gold particles inside the borders of the ribbon (dark blue), while the relative distances >1 (d_o) represent gold particles bound to the surface of the ribbon (light green). Abbreviations: G6F4 = grid labelled with 6F4, G2D9 = grid labelled with 2D9, d_{rel} = relative distance.

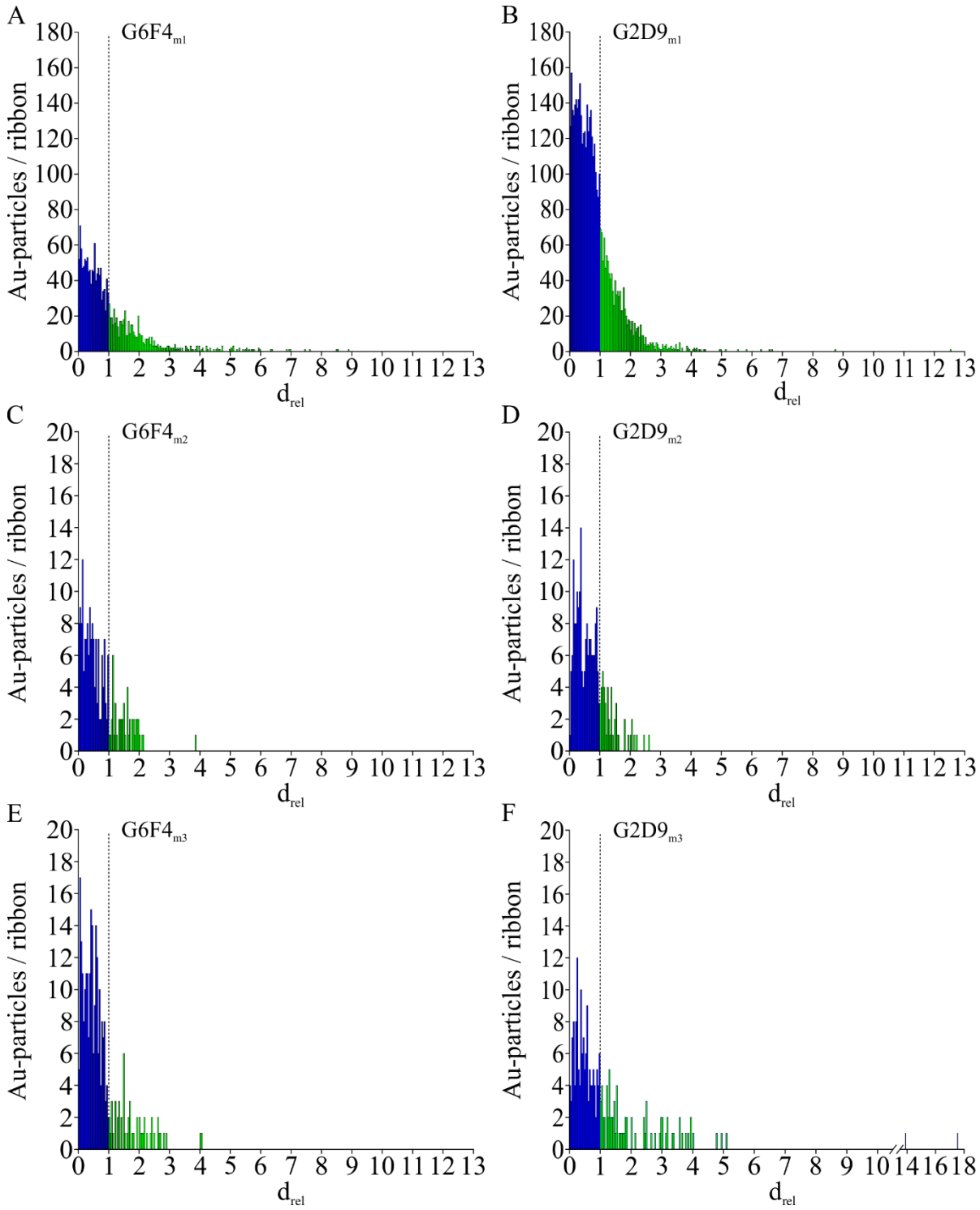

Figure 13: Histograms of the 3 analysed mice, showing the number of gold particles for each relative distance for each of the mice for the grids labelled with 6F4 and the grids labelled with 2D9: The relative distances from 0 to 1 (d_i) represent gold particles inside the borders of the ribbon (dark blue), while the relative distances >1 (d_o) represent gold particles bound to the surface of the ribbon (light green). Abbreviations: G6F4 = grid labelled with 6F4, G2D9 = grid labelled with 2D9, d_{rel} = relative distance, m1 = mouse 1, m2 = mouse 2, m3 = mouse 3.

3.4 Statistical Analysis

Outliers were first noticed in the histograms and then visualized in box plots. One outlier in the 2D9 grid 1 of mouse 1 (m1) and two outliers in the 2D9 grid of mouse 3 (m3) were identified and confirmed by the non-parametric Walsh outlier test. While in the box plots there are far more technical outliers visible, because they are above the 95th percentile, only the three outliers in these two grids were considered for exclusion, as they are visibly standing out and shift the mean value, which can be seen as the thicker line in the box plots, noticeably.

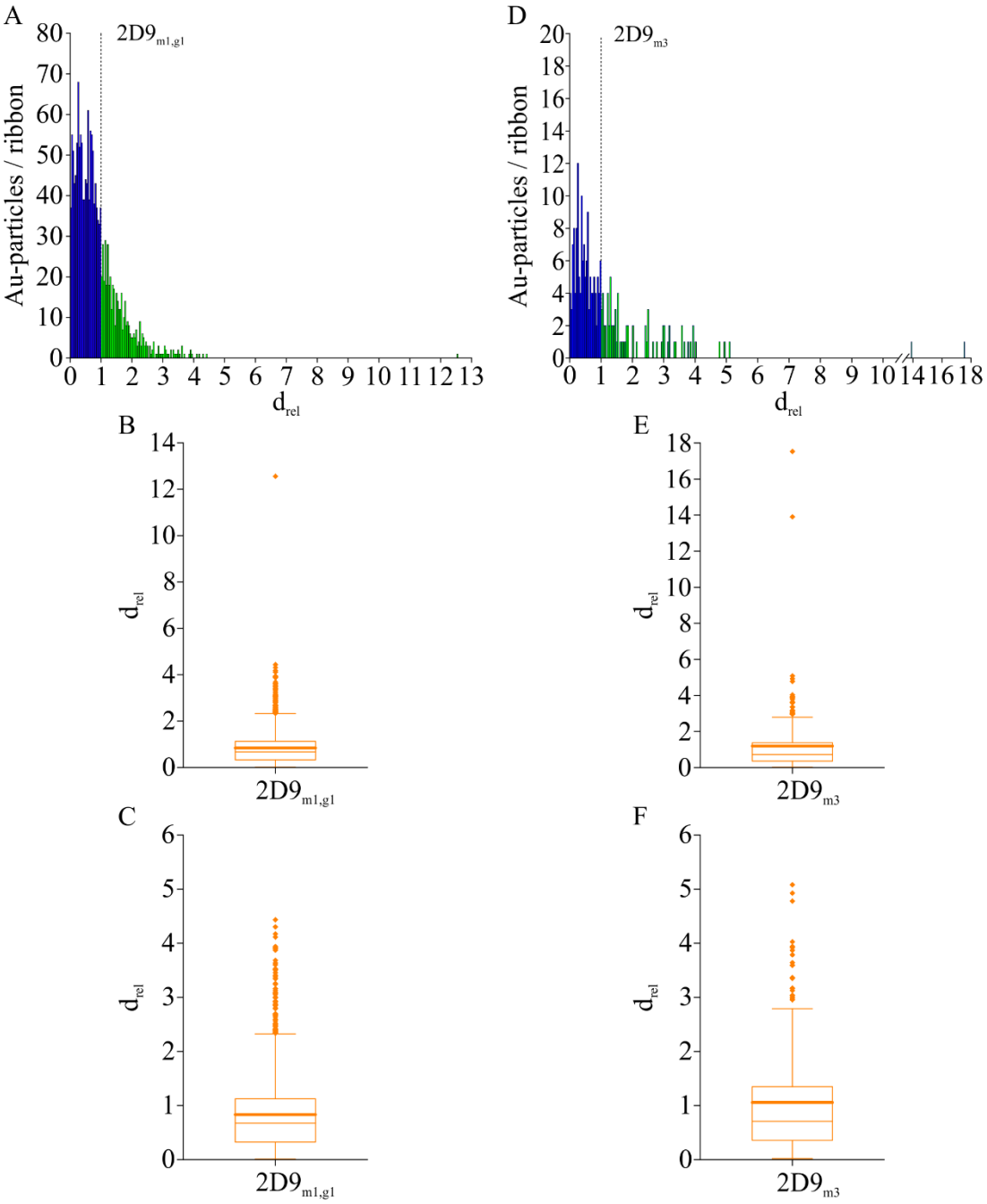

Figure 14: Identification and exclusion of outliers in 2D9-graph1 (A-C) of m1 and 2D9-graph of m3 (D-F): A and D show the histograms with the outliers, B and E the box plot with the outliers, and C and F the box plot after the exclusion of the outliers. The mean value is shown for each box plot in a thick line, the median is displayed as a thinner line. Abbreviations: G6F4 = grid labelled with 6F4, G2D9 = grid labelled with 2D9, d_{rel} = relative distance, g1 = grid 1, m1 = mouse 1, m3 = mouse 3.

First the statistical analysis of the relative distances of the six grids from mouse 1 (m1) was done, after that, both m2 and m3 were analyzed separately (see below).

In the histograms in Figure 12 showing the results of the topographical analysis of mouse 1 (m1) it becomes apparent that distribution of the gold particles is very similar in both antibodies, 6F4 and 2D9. To confirm this, logistic graphs were superimposed over all six histograms of m1 as distribution curves, depicting not the absolute number of gold particles at a given relative distance, but laying the focus on the distribution of the gold particles on the ribbon and therefore the distribution of the two RIBEYE Domains across the width of the ribbon.

Like already seen in the histograms above, the number of gold particles declines the higher the distance from the midline. All distribution graphs show a very similar shape. The highest amount of gold particles is found close to the midline ($d_{rel} = 0$). Coming closer to the border of the ribbon ($d_{rel} = 1$), the number of gold particles starts to generally decrease first slowly and then quite quickly. Outside the borders of the synaptic ribbon, i.e. on the surface of the ribbon, this trend continues. To get a better image of the distribution of the gold particles inside the borders of the synaptic ribbon, meaning the distribution of the two RIBEYE Domains in the core of the ribbon, another histogram was prepared for each of the six grids of mouse 1, depicting just the numbers of gold particles at the relative distances from zero to one shown in Figure 15. Again the same tendency can be seen for all of the grids.

The rate of change of each of the distribution curves was then demonstrated for each antibody and each of its grids by calculating the 1st derivative of the function values of the distribution graph and inverting the graph for a better visualization (Figure 17 & Figure 18). While the point of highest change is not always located at the same relative distance, this shows that overall all distribution graphs have a similar rate of change, which means that the distribution of gold particles and therefore the RIBEYE Domains follows the same trends.

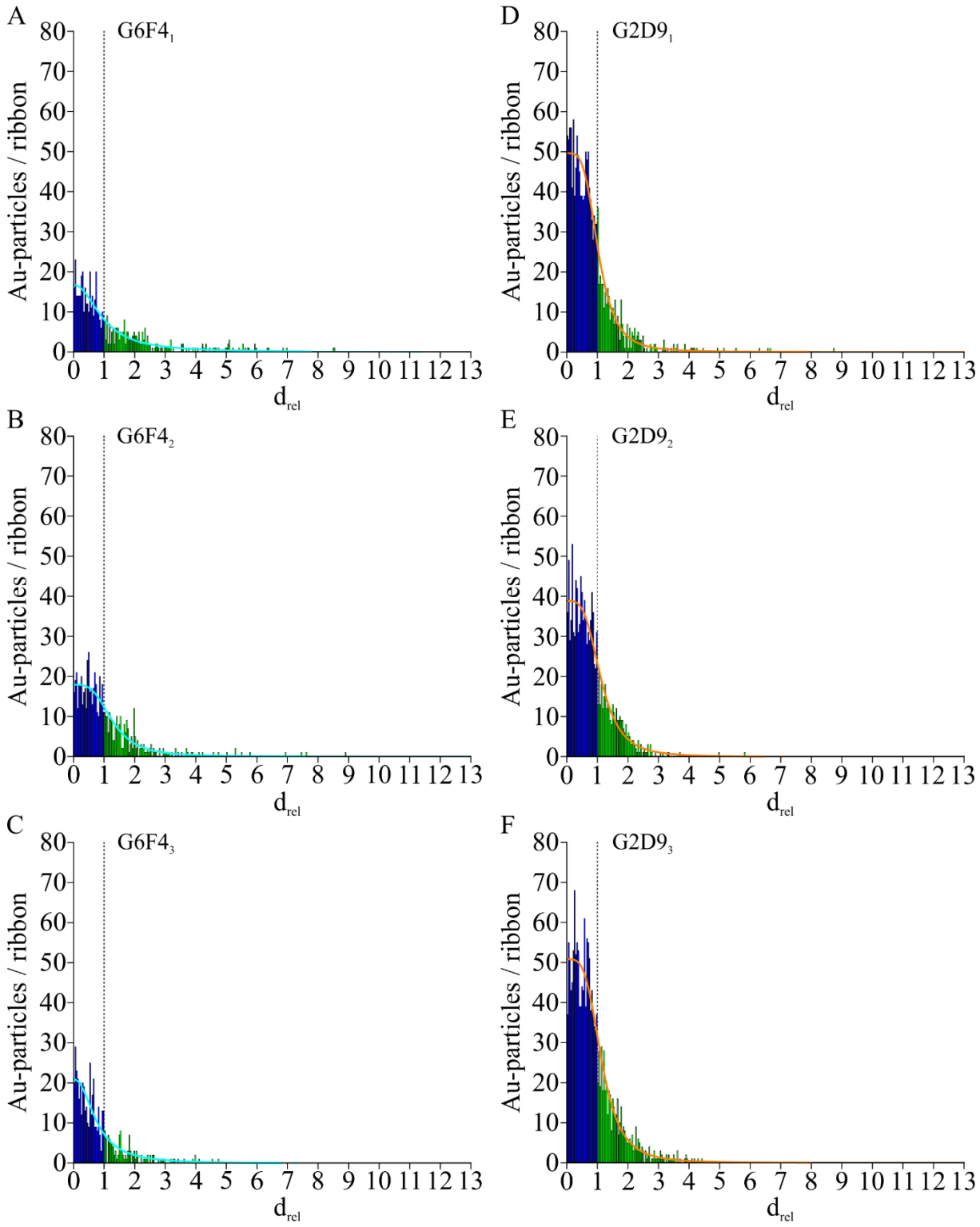

Figure 15: Histograms with logistic graphs functioning as distribution curves for mouse 1 for the three grids labelled with 6F4 (A-C) and the three grids labelled with 2D9 (D-F): The relative distances from 0 to 1 (d_i) represent gold particles inside the borders of the ribbon (dark blue), while the relative distances >1 (d_o) represent gold particles bound to the surface of the ribbon (light green). The distribution curves are superimposed on all histograms for 6F4 in turquois, for 2D9 in orange. Abbreviations: G6F4 = grid labelled with 6F4, G2D9 = grid labelled with 2D9, d_{rel} = relative distance.

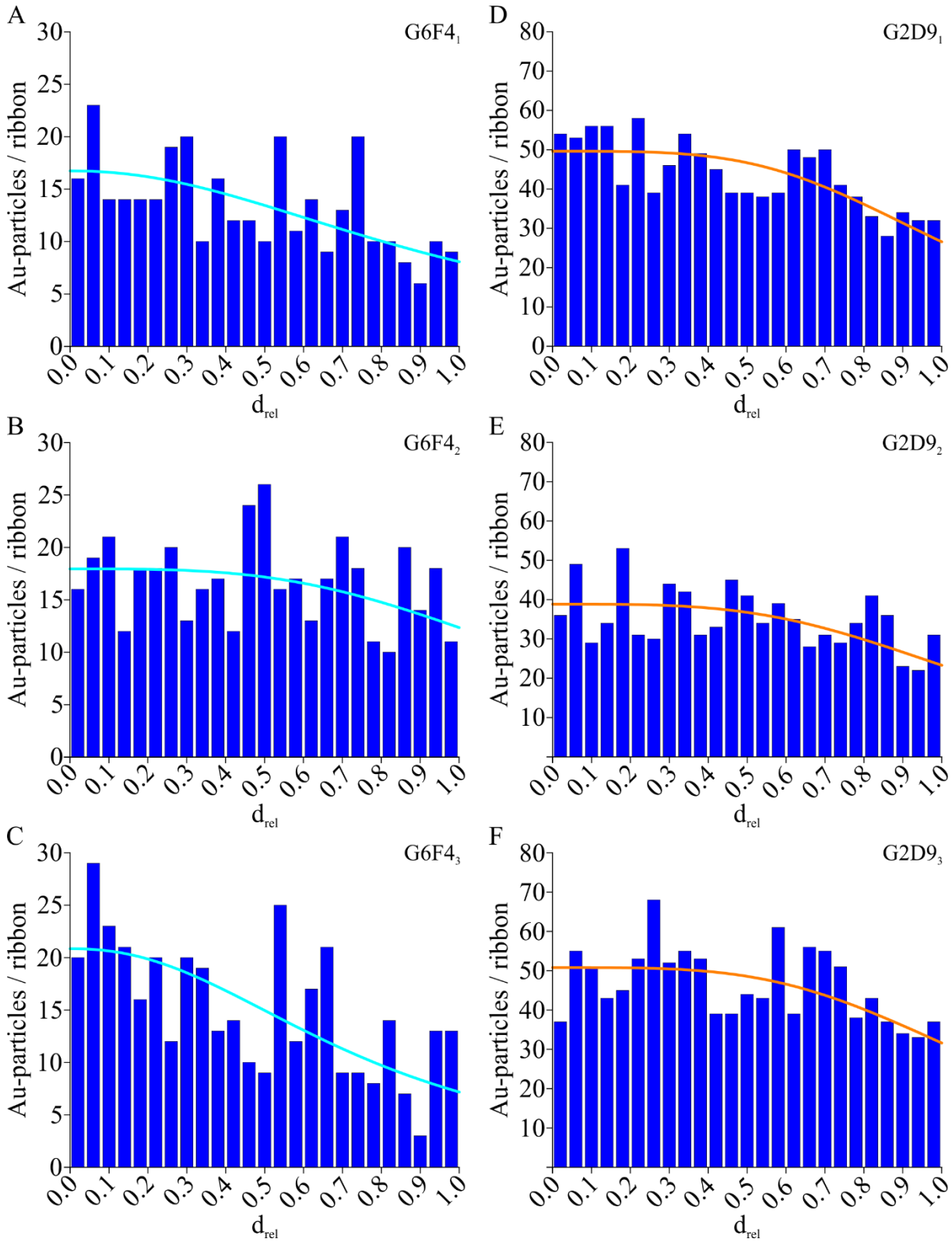

Figure 16: Partial histograms of d_{rel} 0-1 with superimposed distribution graphs for the 3 6F4-grids (A-C) and the 3 2D9-grids (D-F) of mouse 1: The relative distances from 0 to 1 (d_i) represent gold particles inside the borders of the ribbon in dark blue. The distribution curves are superimposed on all histograms for 6F4 in turquois, for 2D9 in orange. Abbreviations: G6F4 = grid labelled with 6F4, G2D9 = grid labelled with 2D9, d_{rel} = relative distance.

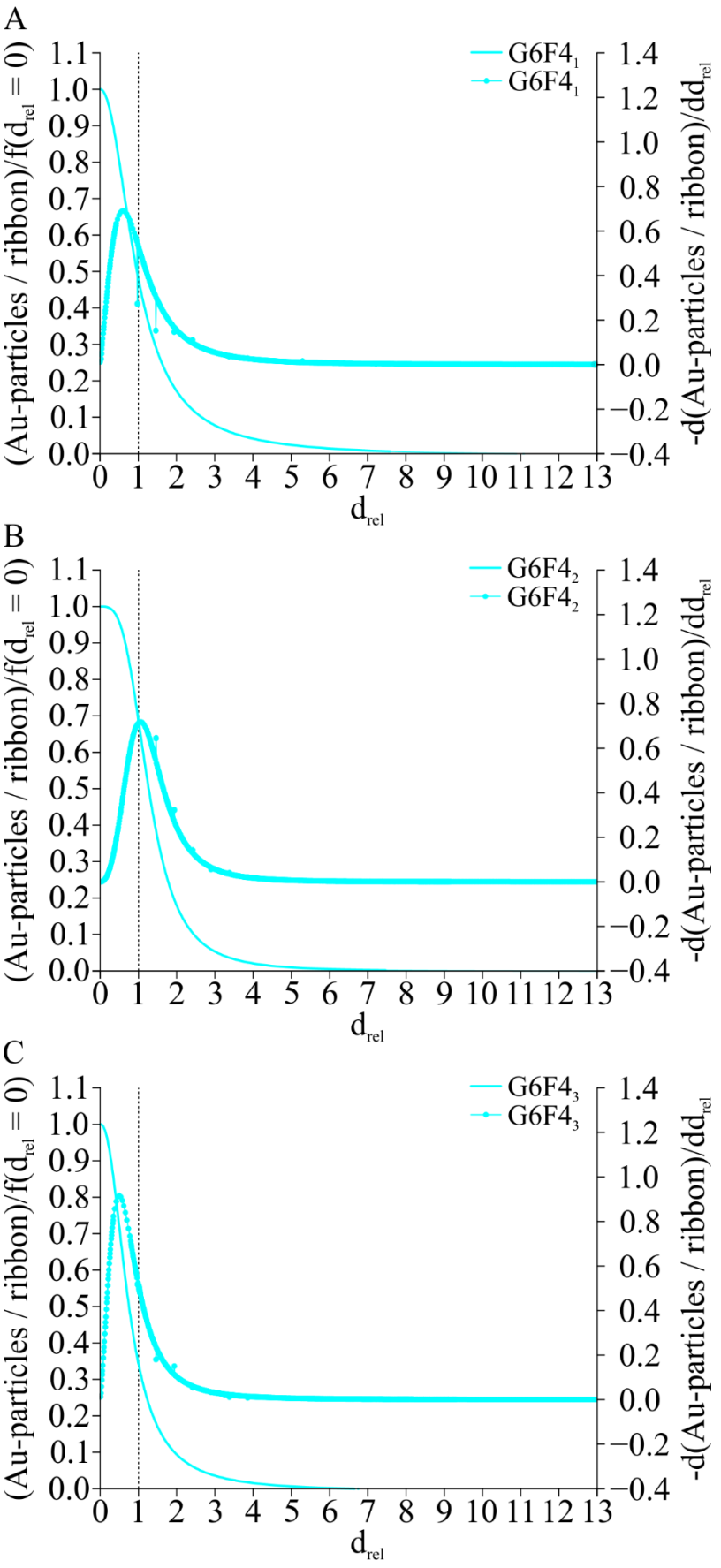

Figure 17: Distribution graphs of 6F4-grids 1-3 of mouse 1 and the inverted rate of change graph: The rate of change is calculated with the 1st derivative of each value of the distribution graph. Abbreviations: G6F4 = grid labelled with 6F4, G2D9 = grid labelled with 2D9, d_{rel} = relative distance, d/dd = first derivative.

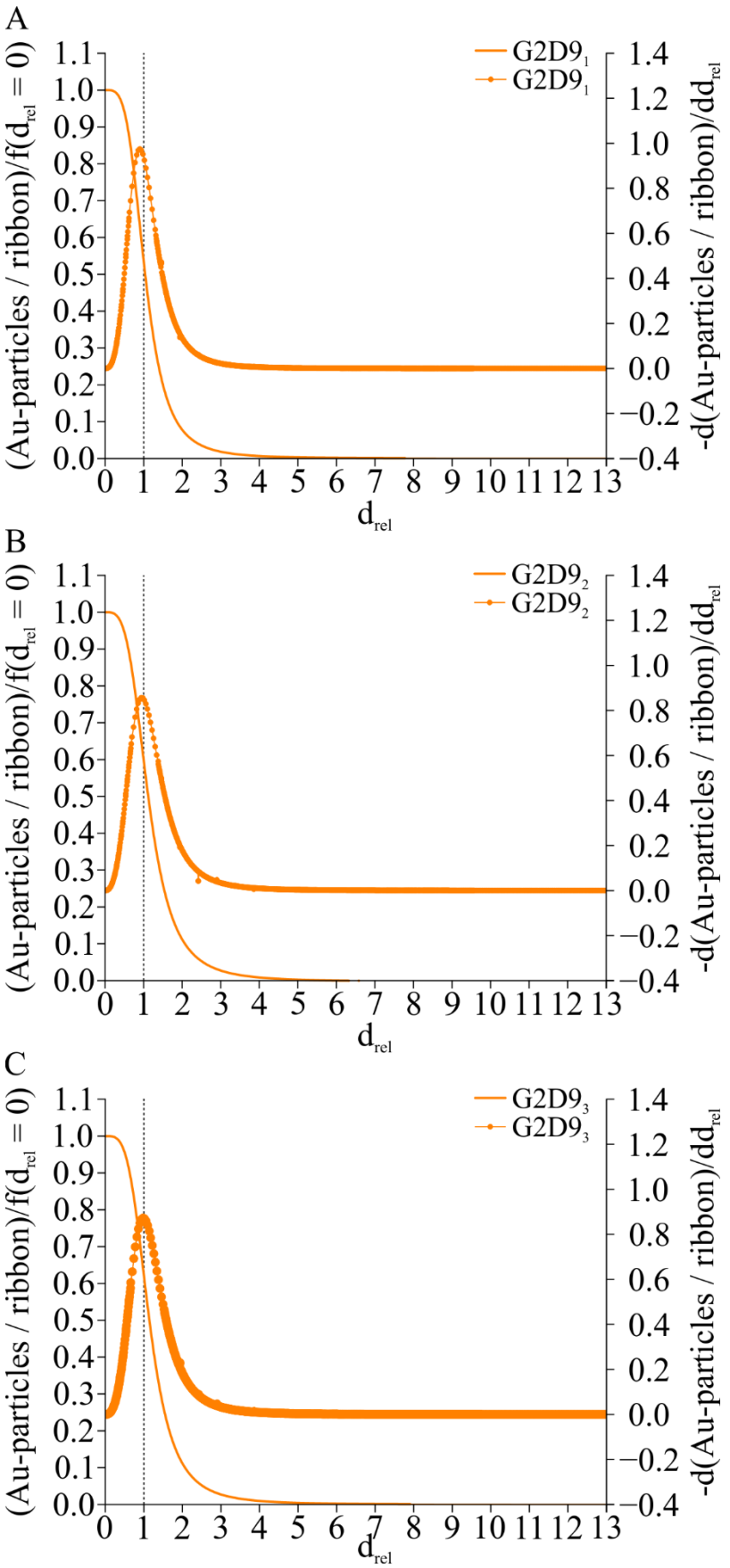

Figure 18: Distribution graphs of 2D9-grids 1-3 of mouse 1 and the inverted rate of change graph: The rate of change is calculated with the 1st derivative of each value of the distribution graph. Abbreviations: G6F4 = grid labelled with 6F4, G2D9 = grid labelled with 2D9, d_{rel} = relative distance, d/dd = first derivative.

The three grids of mouse 1 (m1) labelled with 6F4 were combined into a single histogram. The same was done with the three 2D9-labelled grids of m1 and a distribution graph was superimposed on each of them (Figure 19).

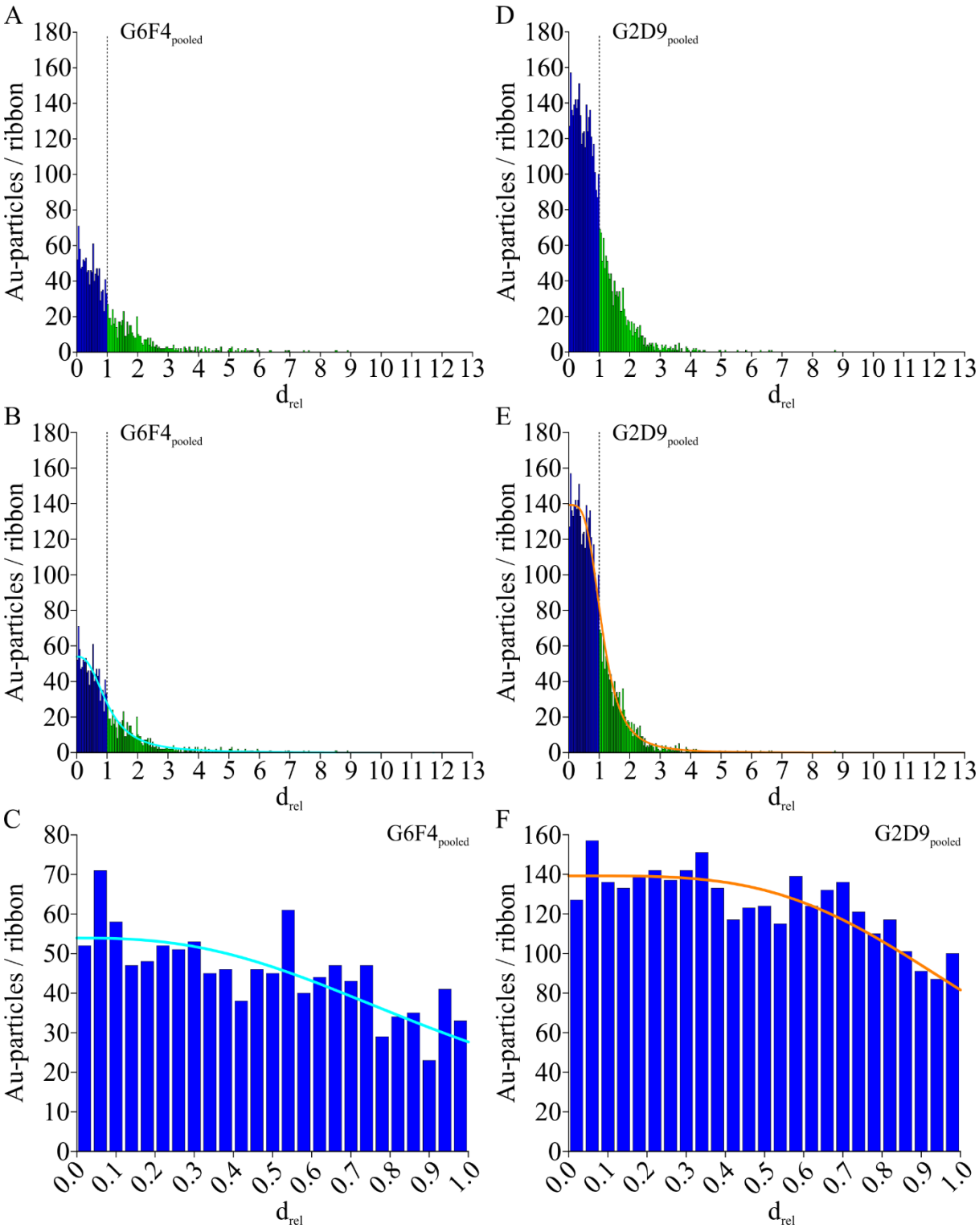

Figure 19: Histograms of the pooled 6F4- and 2D9-grids of <u>mouse 1</u> (A&D), the same histograms with superimposed distribution curves (B&E), and the partial histograms of d_{rel} 0-1 with superimposed distribution graphs: The relative distances from 0 to 1 (d_i) represent gold particles inside the borders of the ribbon (dark blue), while the relative distances >1 (d_o) represent gold particles bound to the surface of the ribbon (light green). The distribution curves are superimposed on all histograms for 6F4 in turquois, for 2D9 in orange. Abbreviations: G6F4 = grid labelled with 6F4, G2D9 = grid labelled with 2D9, d_{rel} = relative distance.

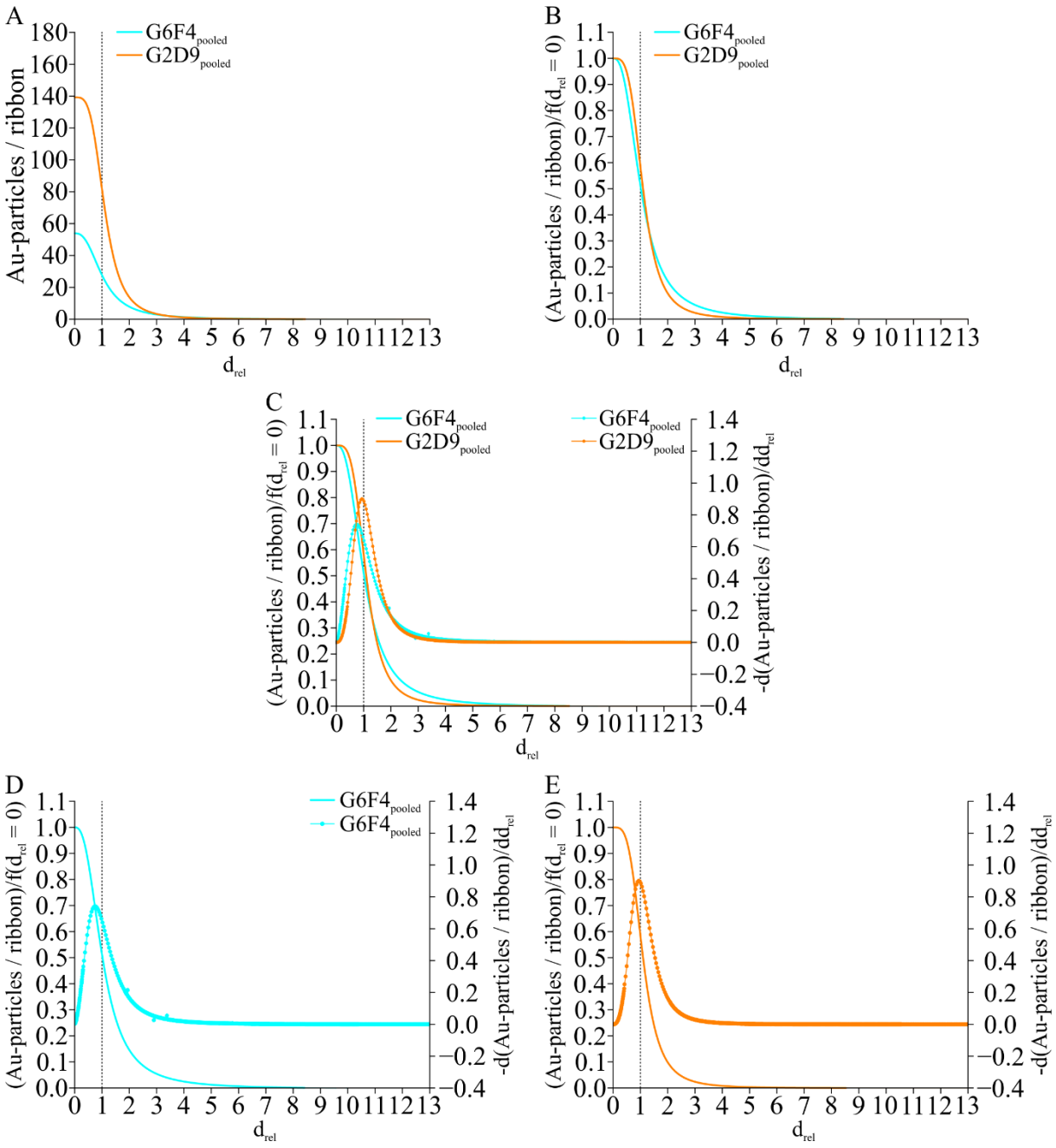

Figure 20: Comparison of the two distribution graphs of the 6F4-grids pooled (turquois) and the 2D9-grids pooled (orange) for <u>mouse 1</u>: A: The distribution curves compared on top of each other. B: The distribution curves both normalized to the starting value f(d_{rel} = 0) for better comparison. C: the normalized distribution graphs superimposed on each other with their rate of change curves. D: The distribution graph with the rate of change curve of the pooled 6F4-grids of mouse 1. E: The distribution graph with the rate of change curve of the pooled 2D9-grids of mouse 1. Abbreviations: G6F4 = grid labelled with 6F4, G2D9 = grid labelled with 2D9, d_{rel} = relative distance, d/dd = first derivative.

Of course the pooled results confirm what was already seen as trends in the individual grids of m1 (see above), as they looked already very similar to each other. Again the relative distances from zero to one were plotted into an extra histogram with another overlying distribution graph, confirming the tendency that the further away from the midline of the synaptic ribbon, the less gold particles are found even just in the core of the ribbon. As visible in Figure 19, all

distribution graphs show no large noticeable differences in shape, suggesting that the distribution of both RIBEYE Domains is very similar. Moreover, this was confirmed by laying the two distribution graphs on top of each other and normalizing all their values to the starting value d_{rel0} (Figure 20). It can be concluded that in this mouse the distribution of the RIBEYE A- and B-Domain is nearly equal.

To confirm the results, the statistical analysis of the other two mice followed. Even though much less data was analyzed, because only one grid per antibody was evaluated for each mouse, the results are very similar. The histograms and their distribution graphs are very similar in shape with the number of particles per relative distances declining the further away from the midline of the synaptic ribbon they are located. This can also be seen in the histograms and distribution graphs of the core of the ribbon. The normalized distribution graphs of the two RIBEYE antibodies 6F4 and 2D9 are a bit more divergent in mouse 2 and 3 than the distribution graphs of mouse 1, but this can be attributed to the fact that much less gold particles were analyzed in either of these mice compared to mouse 1 (see below, Table 2) and the final pooled results of all mice (see below) don´t indicate that there are significant differences between the two RIBEYE antibodies.

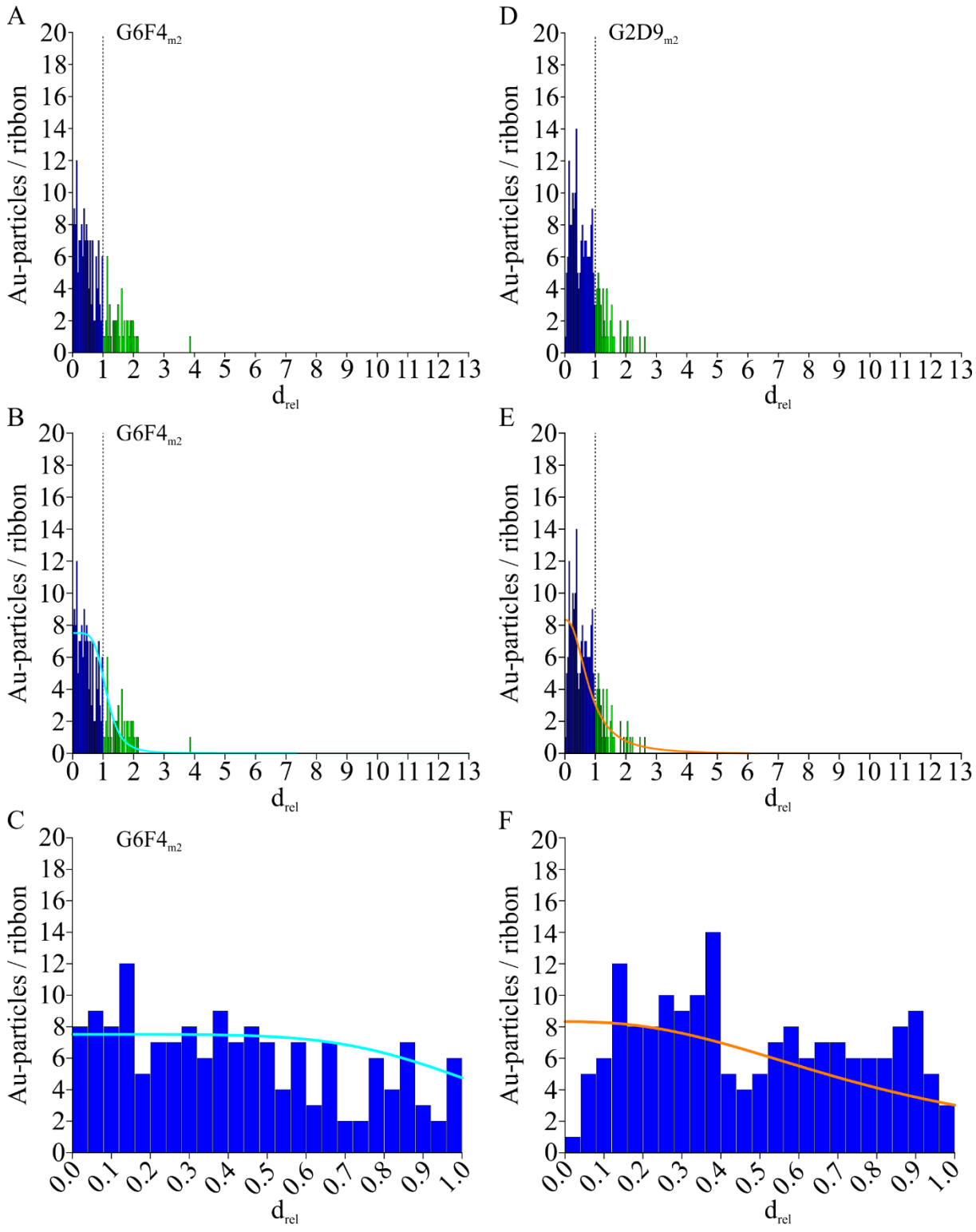

Figure 21: Histograms of the 6F4- and 2D9-grids of <u>mouse 2</u> (A&D), the same histograms with superimposed distribution curves (B&E), and the partial histograms of d_{rel} 0-1 with superimposed distribution graphs: The relative distances from 0 to 1 (d_i) represent gold particles inside the borders of the ribbon (dark blue), while the relative distances >1 (d_o) represent gold particles bound to the surface of the ribbon (light green). The distribution curves are superimposed on all histograms for 6F4 in turquois, for 2D9 in orange. Abbreviations: G6F4 = grid labelled with 6F4, G2D9 = grid labelled with 2D9, d_{rel} = relative distance, m2 = mouse 2.

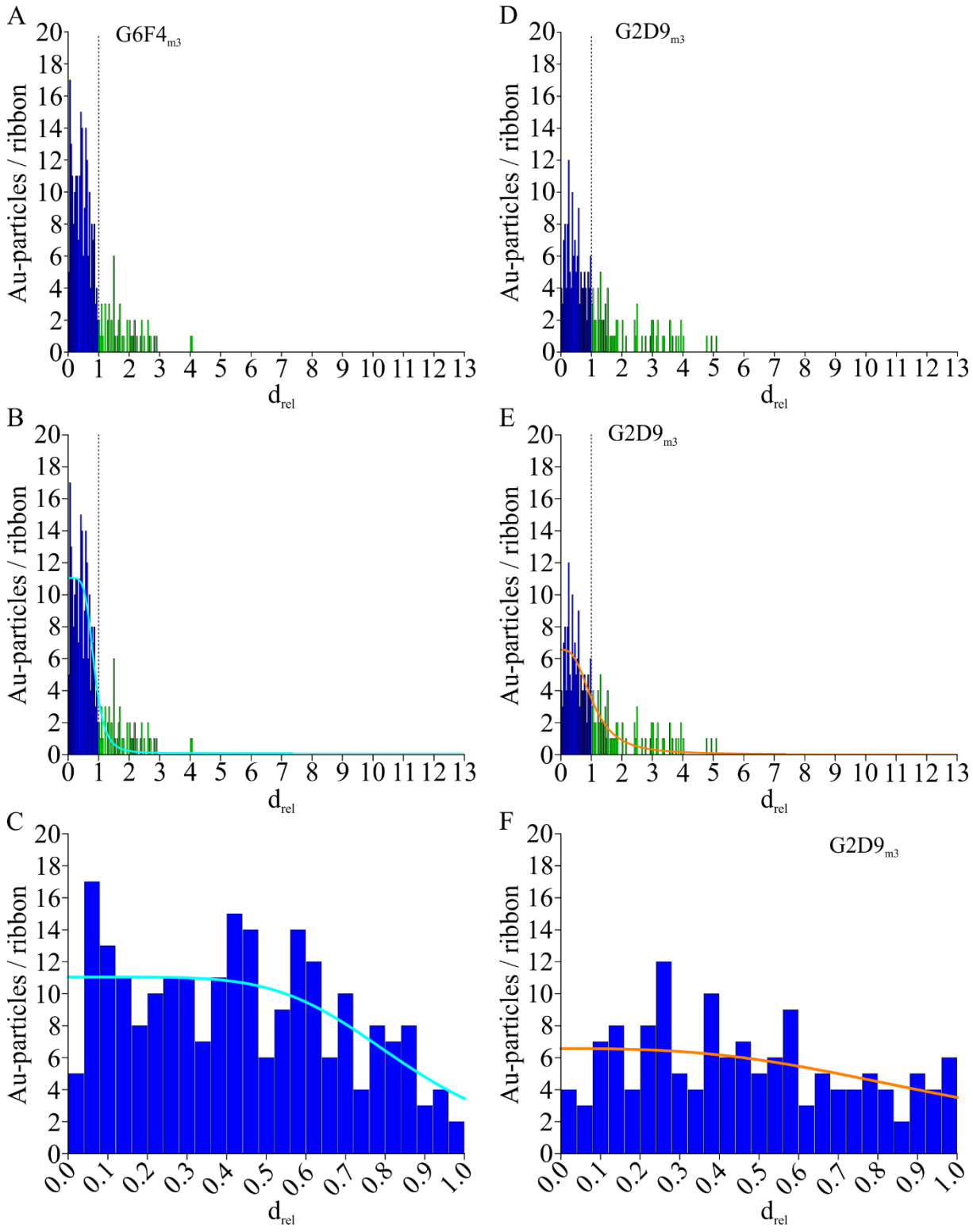

Figure 22: Histograms of the 6F4- and 2D9-grids of <u>mouse 3</u> (A&D), the same histograms with superimposed distribution curves (B&E), and the partial histograms of d_{rel} 0-1 with superimposed distribution graphs: The relative distances from 0 to 1 (d_i) represent gold particles inside the borders of the ribbon (dark blue), while the relative distances >1 (d_o) represent gold particles bound to the surface of the ribbon (light green). The distribution curves are superimposed on all histograms for 6F4 in turquois, for 2D9 in orange. Abbreviations: G6F4 = grid labelled with 6F4, G2D9 = grid labelled with 2D9, d_{rel} = relative distance, m3 = mouse 3.

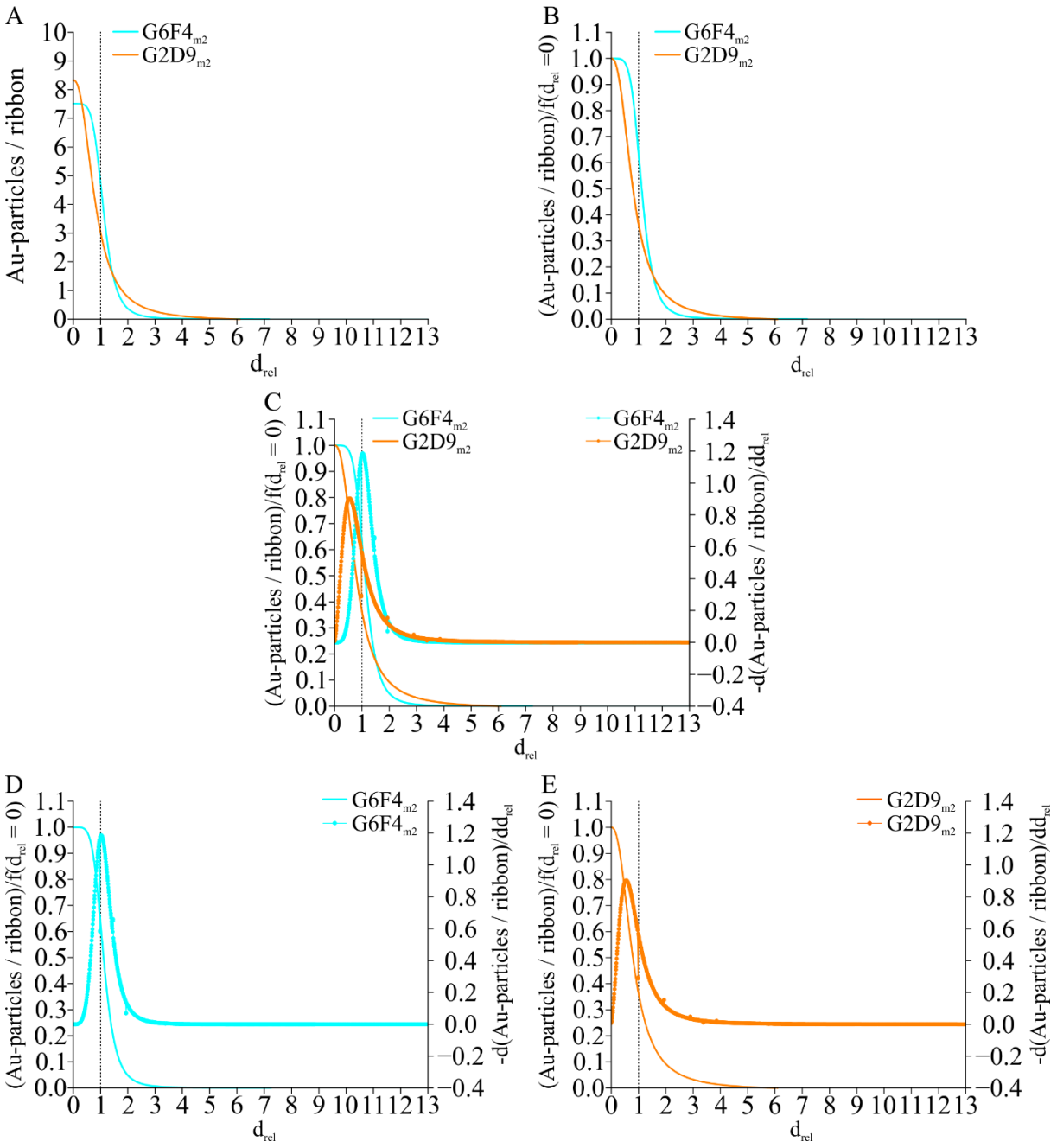

Figure 23: Comparison of the two distribution graphs of the 6F4-grid (turquois) and the 2D9-grid (orange) for <u>mouse 2</u>: A: The distribution curves compared on top of each other. B: The distribution curves both normalized to the starting value f(d_{rel} = 0) for better comparison. C: the normalized distribution graphs superimposed on each other with their rate of change curves. D: The distribution graph with the rate of change curve of the 6F4-grid of mouse 2. E: The distribution graph with the rate of change curve of the 2D9-grid of mouse 2. Abbreviations: G6F4 = grid labelled with 6F4, G2D9 = grid labelled with 2D9, d_{rel} = relative distance, m2 = mouse 2, d/dd = first derivation.

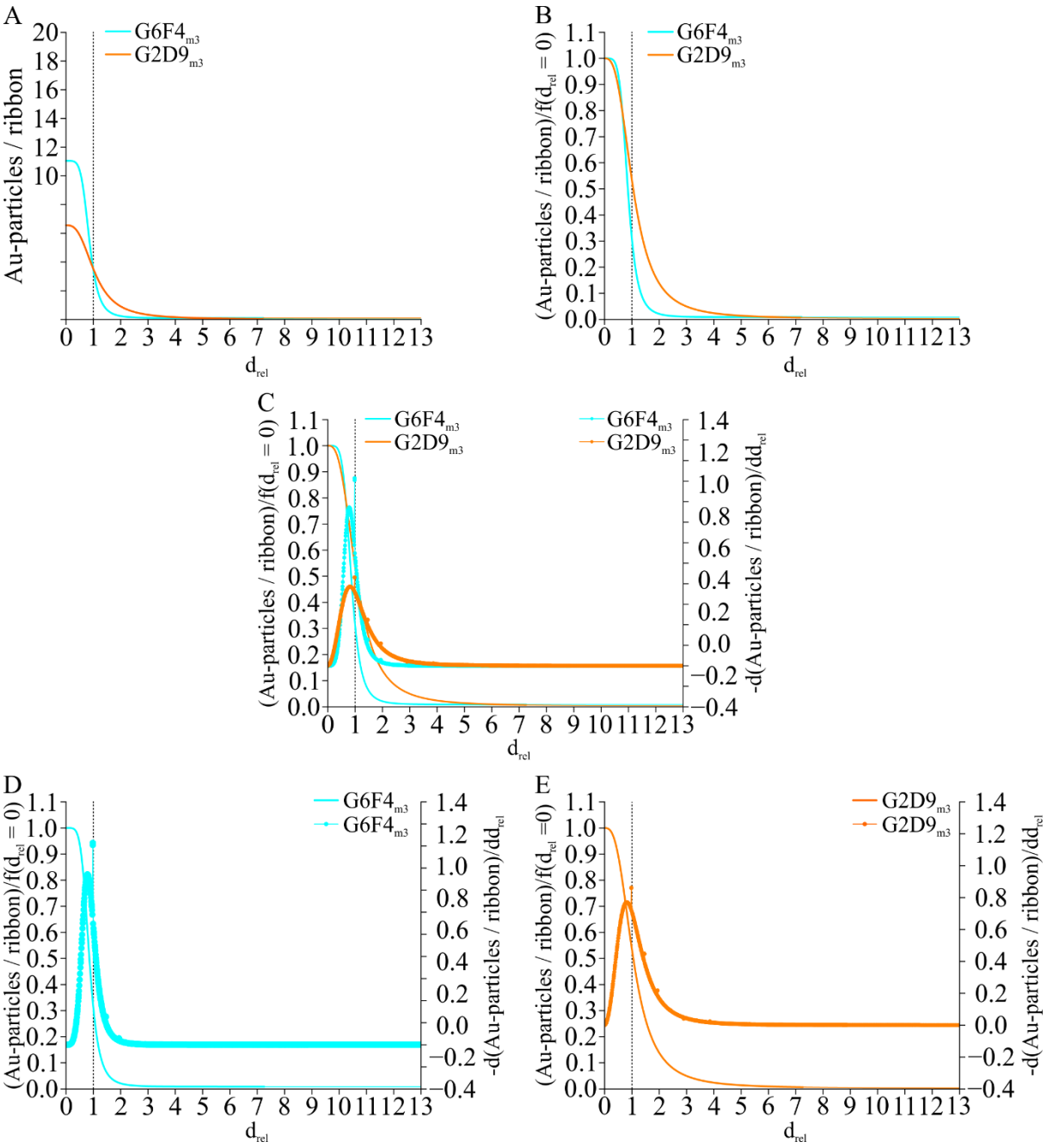

Figure 24: Comparison of the two distribution graphs of the 6F4-grid (turquois) and the 2D9-grid (orange) for <u>mouse 3</u>. A: The distribution curves compared on top of each other. B: The distribution curves both normalized to the starting value f(d_{rel} = 0) for better comparison. C: the normalized distribution graphs superimposed on each other with their rate of change curves. D: The distribution graph with the rate of change curve of the 6F4-grid of mouse 3. E: The distribution graph with the rate of change curve of the 2D9-grid of mouse 3. Abbreviations: G6F4 = grid labelled with 6F4, G2D9 = grid labelled with 2D9, d_{rel} = relative distance, m3 = mouse 3, d/dd = first derivation.

Table 1 and Table 2 show the number of ribbons analyzed per grid and per mouse and the number of gold particles analyzed per grid and per mouse. This emphasizes the weighting of the different mice in the final result, as for mouse 2 and 3 far less ribbons and gold particles were analyzed. The affinity of 6F4 and 2D9, visible as the number of gold particles per ribbon, is different for mouse 1, than it is for mouse 2 and 3, as the latter were prepared in a

separate experiment and the number of gold particles per ribbon is dependent on the aliquot of purified antibody that was used in a given experiment.

Table 1: Number of ribbons and gold particles analyzed per ribbon for both antibodies in each of the grids of mouse 1

Mouse 1	6F4	2D9
Grid1	40 ribbons 555 gold particles 13,9 gold particles/ribbon	44 ribbons 1459 gold particles 33,1 gold particles/ribbon
Grid2	48 ribbons 659 gold particles 13,7 gold particles/ribbon	47 ribbon 1219 gold particles 25,9 gold particles/ribbon
Grid3	37 ribbons 503 gold particles 13,6 gold particles/ribbon	53 ribbons 1645 gold particles 31,0 gold particles/ribbon

Table 2: Number of ribbons and gold particles analyzed per ribbon for both antibodies for each of the 3 mice

All mice	6F4	2D9
Mouse 1	125 ribbons 1717 gold particles 13,7 gold particles/ribbon	144 ribbons 4323 gold particles 30,0 gold particles/ribbon
Mouse 2	38 ribbons 224 gold particles 5,9 gold particles/ribbon	37 ribbons 203 gold particles 5,5 gold particles/ribbon
Mouse 3	38 ribbons 280 gold particles 7,4 gold particles/ribbon	34 ribbons 219 gold particles 6,4 gold particles/ribbon

When the results of all three mice were once again combined to form the final pooled results (Figure 25 and Figure 26), it became evident that the RIBEYE A-Domain, labelled with 6F4, and the RIBEYE B-Domain, labelled with 2D9, have nearly equal distributions across the width of the ribbon. This trend was already visible in the very first grids of mouse 1 and continued for all following comparisons between the antibodies. It was again confirmed visually in the normalized distribution graphs on top of each other, which are nearly congruent, and the rate of change graphs, which show slightly different points of maximal change, but also confirm overall, that RIBEYE A and B distribution is almost equal.

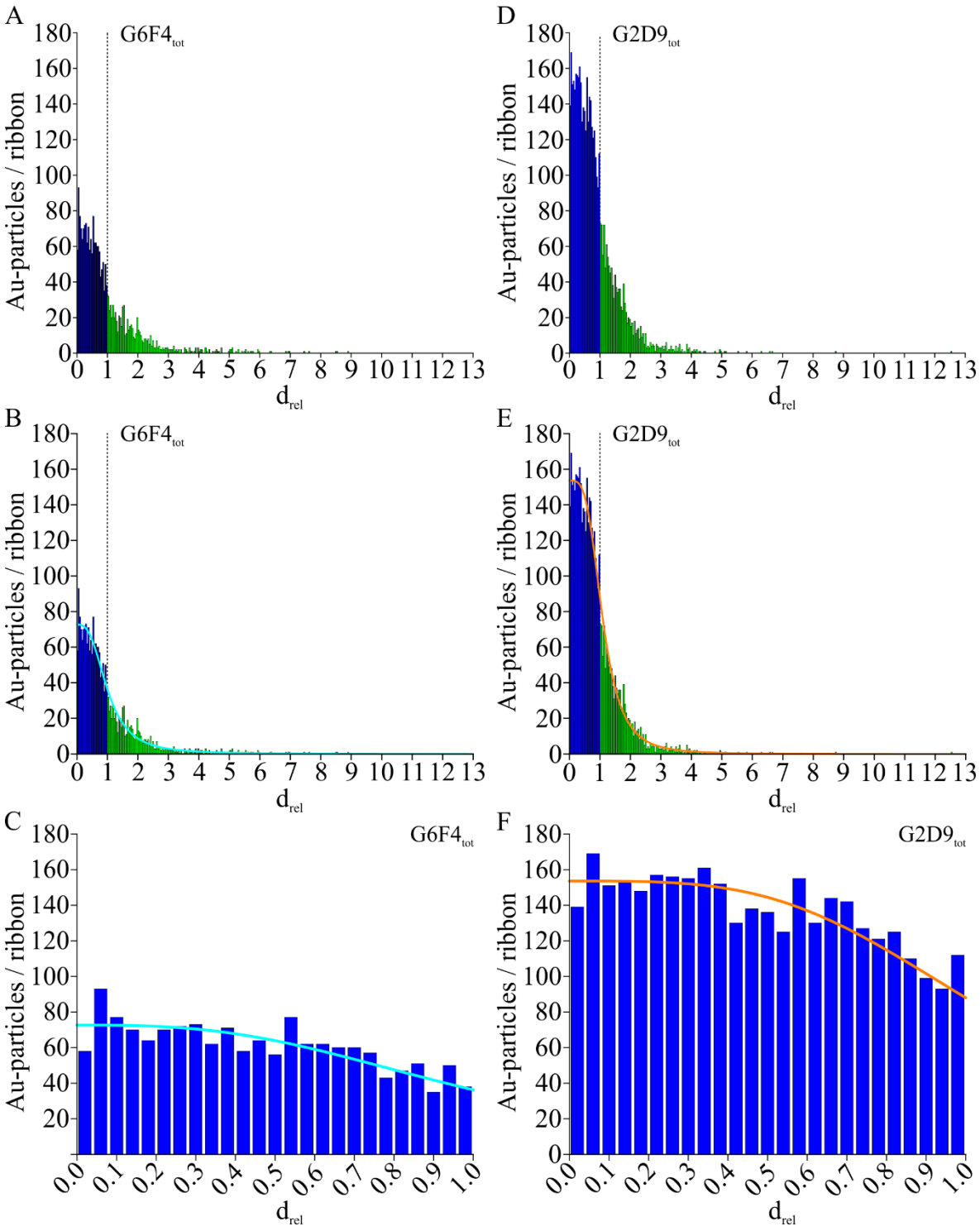

Figure 25: Histograms of the 6F4- and 2D9-grids of <u>all mice pooled</u> (A&D), the same histograms with superimposed distribution curves (B&E), and the partial histograms of d_{rel} = 0-1 with superimposed distribution graphs: The relative distances from 0 to 1 (d_i) represent gold particles inside the borders of the ribbon (dark blue), while the relative distances >1 (d_o) represent gold particles bound to the surface of the ribbon (light green). The distribution curves are superimposed on all histograms for 6F4 in turquois, for 2D9 in orange. Abbreviations: G6F4 = grid labelled with 6F4, G2D9 = grid labelled with 2D9, d_{rel} = relative distance, tot = total.

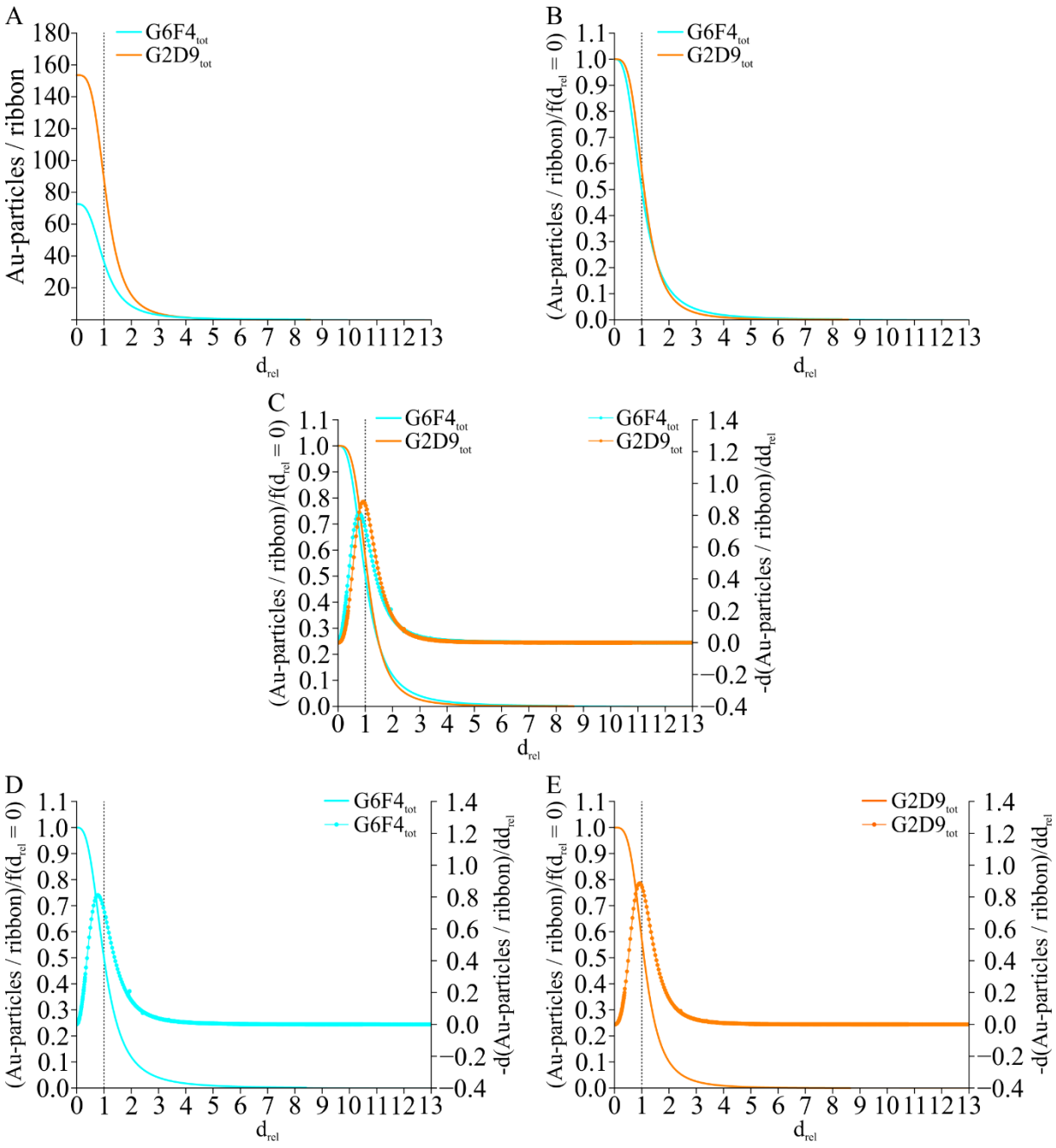

Figure 26: Comparison of the two distribution graphs of the 6F4-grid (turquois) and the 2D9-grid (orange) for <u>all mice pooled</u>: A: The distribution curves compared on top of each other. B: The distribution curves both normalized to the starting value f(d_{rel} = 0) for better comparison. C: the normalized distribution graphs superimposed on each other with their rate of change curves. D: The distribution graph with the rate of change curve of the 6F4-grids of mouse 1-3. E: The distribution graph with the rate of change curve of the 2D9-grids of mouse 1-3. Abbreviations: G6F4 = grid labelled with 6F4, G2D9 = grid labelled with 2D9, d_{rel} = relative distance, tot = total, d/dd = first derivation.

Afterwards, the number of gold particles per ribbon inside the borders of the ribbon (with distances of one or lower (d_i)) was compared to the number of gold particles per ribbon outside the borders of the ribbon (with distances above one (d_o)) with the non-parametric Kruskal-Wallis test followed by post-hoc Dunn´s test. The results are shown as box plots in Figure 27. For each of the six grids of mouse 1, labelled with 6F4 and 2D9, there are two box plots. The dark blue box plot shows the distribution of the number of gold particles per ribbon

inside the borders of the ribbon (i.e. on the surface of the ribbon), while the light green box plot shows the distribution of the number of gold particles per ribbon outside the borders of the ribbon (i.e. on the surface of the synaptic ribbon). While there is a clear tendency visible for all grids, demonstrating larger numbers of gold particles inside than outside the borders of the ribbon, there was a significant difference in four out of the six grids.

All box plots showing the number of gold particles from the three grids labelled with 6F4 were combined to form one box plot and the three grids labelled with 2D9 also, showing the combined results of mouse 1, which prove there are significantly more gold particles in the core than on the surface of the synaptic ribbon. These results were compared with mouse 2 and 3, which also show the same clear difference between numbers of the particles in the core and numbers of the particles on the surface.

The number of gold particles per ribbon inside and outside the borders of the ribbon were again combined for both antibodies, 6F4 and 2D9, for all mice, plotted as box plots and compared by Kruskal-Wallis followed by Dunn´s test. The resulting box plots in Figure 28 demonstrated finally what we have already seen before, that there is a significantly larger number of gold particles per ribbon lying inside the borders of the ribbon than outside the borders, bound to the surface of the ribbon, for both antibodies.

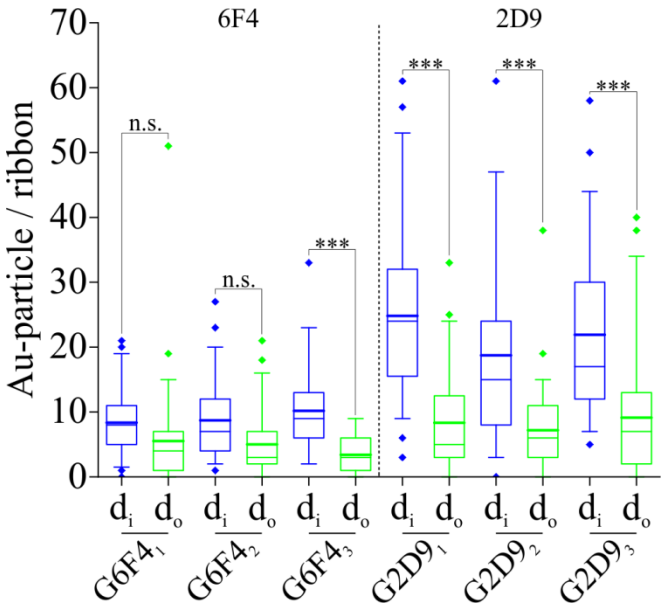

Figure 27: Comparison of the number of gold particles per ribbon inside (dark blue) and outside (light green) the border of the ribbon for each grid: The mean value is shown for each box plot in a thick line, the median is displayed as a thinner line. Abbreviations: G6F4 = grid labelled with 6F4, G2D9 = grid labelled with 2D9, d_i = relative distance of gold particles inside the marked area of the ribbon, d_o = relative distance of gold particles outside the marked area of the ribbon, n.s. = non-significant, *** ≙ $p < 0.001$.

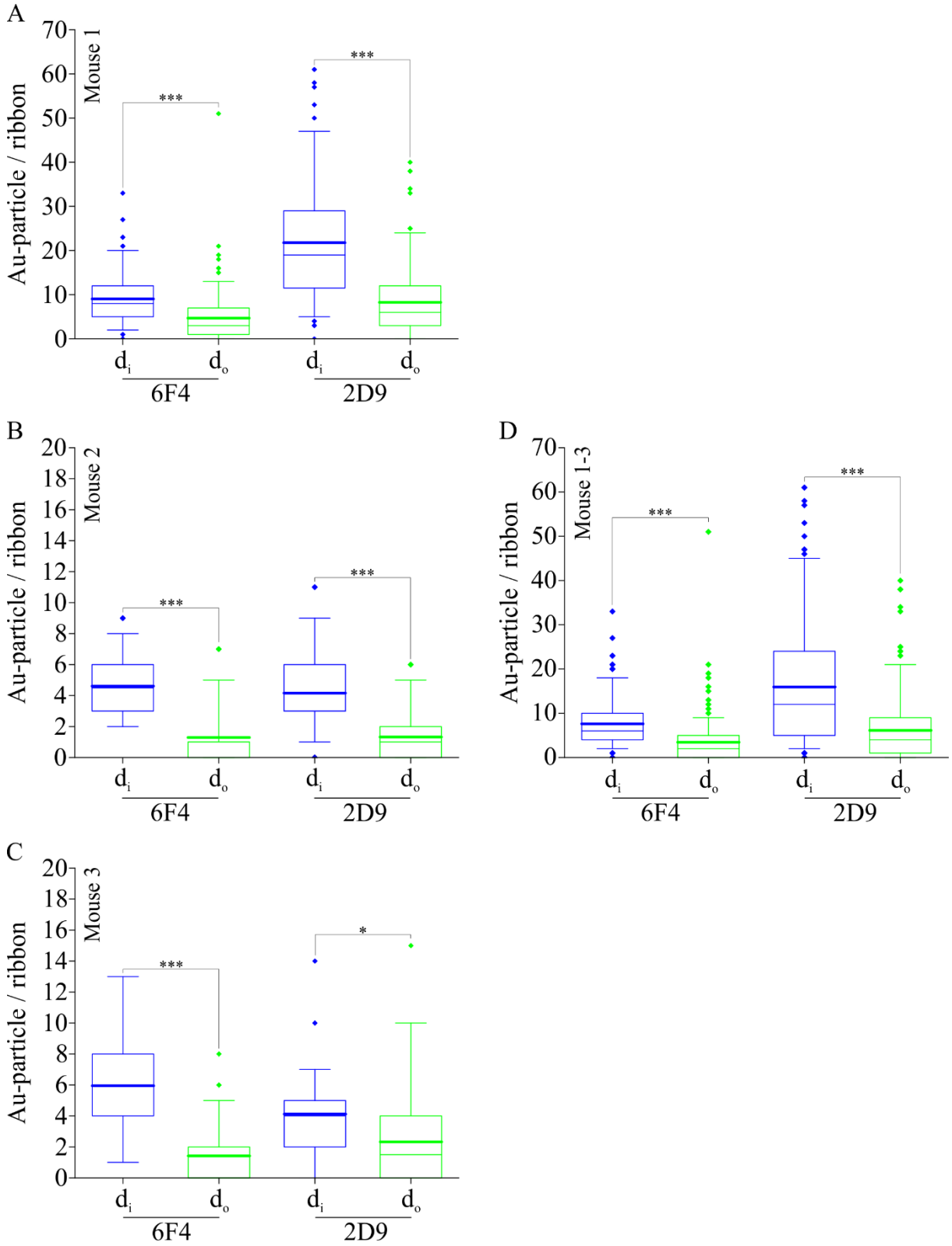

Figure 28: Comparison of the number of gold particles per ribbon inside (dark blue) and outside (light green) the border of the ribbon for each grid: The mean value is shown for each box plot in a thick line, the median is displayed as a thinner line. The number of ribbons that were analyzed is displayed in a number on top of each box plot. Abbreviations: d_i = relative distance of gold particles inside the marked area of the ribbon, d_o = relative distance of gold particles outside the marked area of the ribbon, * ≙ $p < 0.05$, *** ≙ $p < 0.001$.

Next, the percentage of gold particles lying inside the borders of the ribbon in relation to the total number of gold particles analysed on the ribbon was calculated. The same was done with the percentage of gold particles lying outside the border, bound to the surface of the ribbon, in comparison to the total number of gold particles bound to the ribbon. These results were also depicted as a box plot for each mouse separately and for all mice together. The box plots in Figure 29 show the distribution of the percentages of the gold particles lying inside and outside compared to the number of all gold particles per ribbon for both RIBEYE antibodies, 6F4 and 2D9. The two antibodies were compared, and differences between them were analyzed by the non-parametric Kruskal-Wallis test followed by post-hoc Dunn´s test. As shown in Figure 29, there is no significant difference in the percentages of gold particles lying within the borders and the percentage of the gold particles lying outside the borders between the two antibodies. This demonstrates that the two RIBEYE Domains A and B are distributed in a similar way, concerning the number of A- and B-Domains that lay inside the ribbon in relation to the number of those located on the surface of the ribbon.

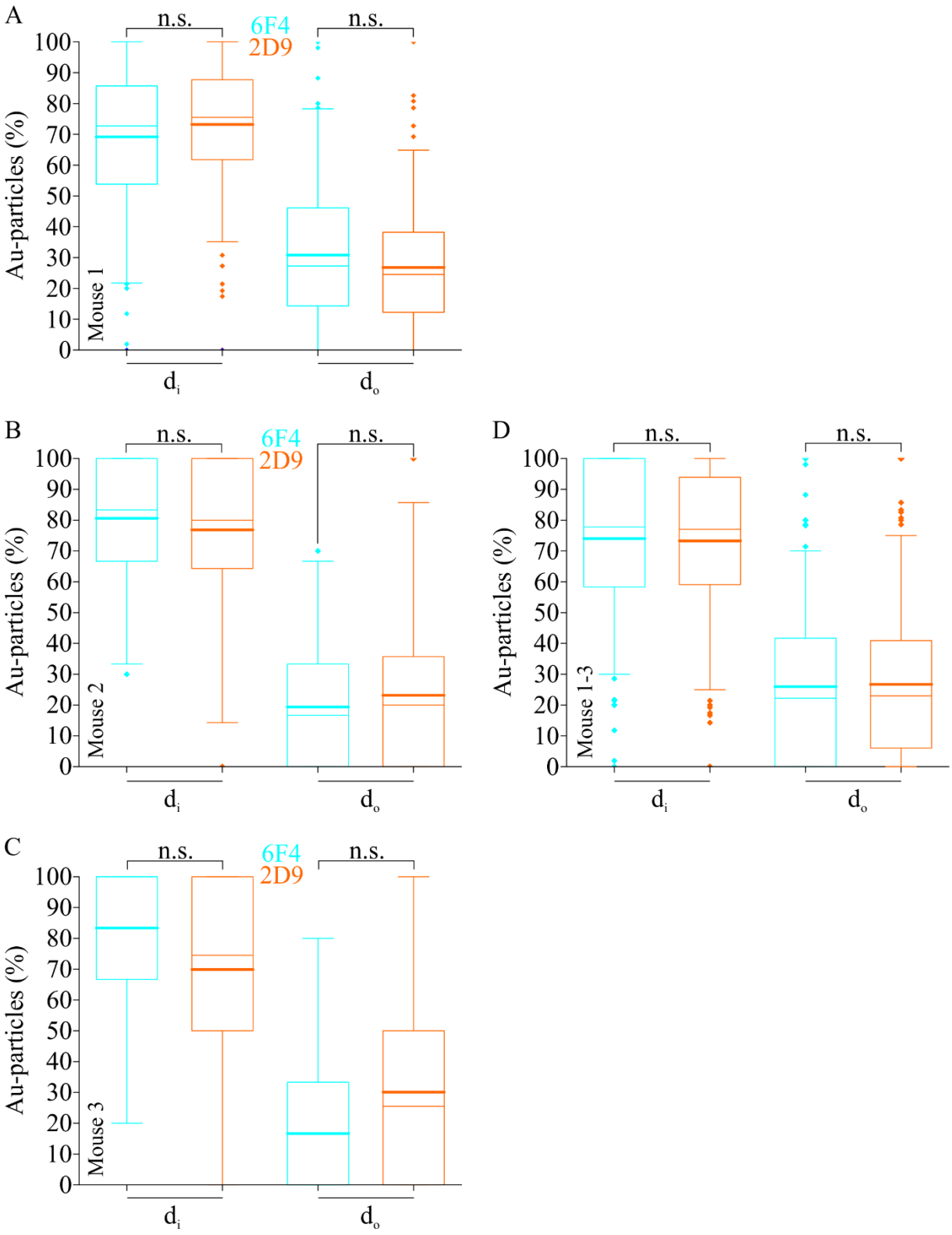

Figure 29: Comparison of the percentages of gold particles laying inside the borders of the ribbon and those bound to the surface, in relation to the number of all gold particles per ribbon: Box plots comparing the percentages of the gold particles per ribbon inside the borders of the ribbon are in dark blue, the light green box plots compare the percentages of gold particles bound to the surface of the ribbon. The mean value is shown for each box plot in a thick line, the median is displayed as a thinner line. Abbreviations: d_i = relative distance of gold particles inside the marked area of the ribbon, d_o = relative distance of gold particles outside the marked area of the ribbon, n.s. = non-significant.

4 Discussion

RIBEYE is known to be a scaffolding protein, which means that the RIBEYE A- and B-Domain can bind to other proteins, including other RIBEYE proteins, and organize with the other bound proteins into a functional unit, the ribbon (Schmitz et al., 2000). RIBEYE is able to self-assemble due to various interaction sites on its A- and B-Domain and does so when heterologously expressed by forming spherical aggregates, which could be the basal unit of a synaptic ribbon (Magupalli et al., 2008). Due to what is known about the function of each of the domains of RIBEYE, it seemed probable that the RIBEYE A-Domains have a structural role and the RIBEYE B-Domains lie on the surface of the synaptic ribbon interacting with several different proteins (Schmitz et al., 2000).

In the present study the distribution of the RIBEYE A- and B-Domain across the width of the synaptic ribbons in photoreceptor ribbon synapses in mice was examined. It was found that the amount of gold particles that mark each RIBEYE Domain at every relative distance from the midline was very similar between the two different antibodies 6F4 (bound to the RIBEYE A-Domain) and 2D9 (bound to the RIBEYE B-Domain). The comparison of the distribution graphs reinforced this finding, because the distribution graphs are nearly congruent. Therefore, it can be concluded that the RIBEYE A-Domain is distributed in a very similar way as the RIBEYE B-Domain and that there are no significant differences in the general location on the width of the synaptic ribbon between RIBEYE A- and B-Domain.

The finding that the location of the RIBEYE A- and B-Domains is very similar on the synaptic ribbon in mouse photoreceptor synapses calls for a revision of the working model hypothesized in 2000 by Schmitz et al. Neither of the domains is located solely on the surface or the core of the ribbon, nor has another protein building the core of the ribbon yet been discovered. Both RIBEYE domains can be found across the whole width including the center of the synaptic ribbon.

The RIBEYE A-Domain was suspected to assume a structural role in the synaptic ribbon for several reasons. The multiple interaction sites were found on the RIBEYE A-Domain and it was discovered that the RIBEYE A-Domain is essential for the building of synaptic ribbons (Magupalli et al., 2008, Maxeiner et al., 2016). Maxeiner et al. proved in 2016 that in the RIBEYE knock-out mouse model the deletion of RIBEYE causes a complete lack of synaptic ribbons and a defect in the ability to release neurotransmitter in a fast and continuous way. But this is also the case for the RIBEYE B-Domain. In 2022 Shankwar et al. discovered that

in RIBEYE knock-in mice, in which the RIBEYE B-Domain was replaced by a fluorescent protein module, ribbons were also absent, proving that the RIBEYE A-Domain alone is not sufficient to build the synaptic ribbon (Shankwar et al., 2022). While it is still possible that the RIBEYE A-Domain has a predominantly structural role, we know now that it is also found on the surface of the ribbon and could therefore have a role in priming vesicles and interacting with the environment of the presynaptic terminal. RIBEYE B-Domain on the other hand has next to its functions of interacting with the proteins of the presynaptic cleft and binding NADH, also a structural function.

The results in the present study were shown in a physiological mouse model and in one specific type of ribbon synapse, the photoreceptor ribbon synapses in the OPL of the retina. It is known that the synaptic ribbon takes many different shapes and sizes dependent on the cell type and species it belongs to. When heterologously expressed, it self-assembles into spherical structures (Magupalli et al., 2008). In rods and cones of mice there are plate-shaped synaptic ribbons (Sterling and Matthews, 2005, Schmitz, 2009). This bears the question how RIBEYE can assemble into the various different shapes of synaptic ribbons it is known to do depending on the cell type it is located in. Another question that arises is which factors in those cell environments cause the synaptic ribbons to assemble into those specific shapes and what purpose the existing differences in shape serve (Magupalli et al, 2008).

When heterologously expressed, RIBEYE assembles into spherical aggregates, which could represent the basic form of ribbons. Because of the many different ways RIBEYE can bind to other RIBYEYE proteins due to its numerous interaction sites on the RIBEYE A- and B-Domain, there are many different possibilities for the scaffolding of RIBEYE into those spheres. On the RIBEYE A-Domain alone there are 3 distinct RIBEYE binding sites, able to bind to binding sites of other RIBEYE A- (homotypic interaction) but also B-Domains (heterotypic interaction) (Magupalli et al., 2008).

It is possible that the synaptic ribbon in rods and cones of mice in certain sections resembles the working model, i.e. that the RIBEYE A-Domains lie closer to the core of the ribbon and the RIBEYE B-Domains are located on the surface of the synaptic ribbon (Schmitz et al., 2000). But in order to match the results of the present study, other sections of the synaptic ribbon would have to differ from the working model, because RIBEYE A-Domains were also found on the surface and RIBEYE B-Domains are also located in the core. The results in the current study don’t show differences in distribution for certain sections of the ribbon, but the

distribution across the ribbon´s width generally, because the ribbon is assessed in only two dimensions, not three.

The methods of direct immunogold labelling in the present study was focused towards finding the most exact location of the RIBEYE antigens as possible for immune electron microscopy, by labelling the primary antibody directly with the colloidal gold, instead of using a secondary antibody labelled with gold. Despite this, the gold naturally still maintains a certain distance from the RIBEYE antigen it is connected to, because of the nature of immunogold labelling. Both, 6F4 and 2D9, are monoclonal IgG antibodies raised against certain amino acid sequences of RIBEYE (Dembla et al., 2018, Shankwar et al., 2022). Because of the variability of the antibody and its hinge region, no exact distance between the gold and the antigen can be stated, but the size of a typical IgG antibody is estimated to be ~ 8.5 nm in height and ~ 13.5 nm between the individual antigen binding sites (Tan et al., 2008). From these estimated dimensions mathematically the distance between the antigen and the gold can therefore be calculated to be ~ 10.8 nm.

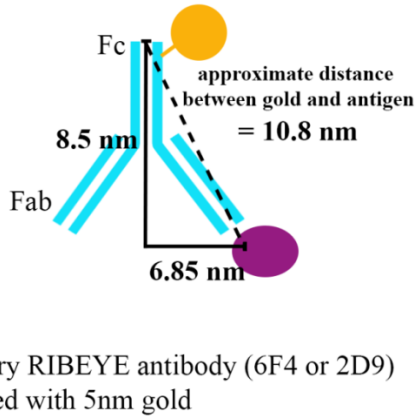

Figure 30: Estimated distance between the gold and the RIBEYE antigen it labels: Schematic representation of a RIBEYE monoclonal IgG antibody. The approximate distance between the antigen and the labelling gold particles was calculated using the Pythagorean Theorem: $(\textbf{Distance between antigen and labelling gold particle})^2 = 8.5^2 + 6.85^2$.

This approximated distance between the gold and the antigen, even though it was reduced as much as possible, gives the method in the present study a certain degree of inaccuracy in resolution. Another source of inaccuracy could be the manual marking of the area of the synaptic ribbon in the electron microscopic images and the manual determination of the midline of the ribbon. Apart from only considering two dimensions of the synaptic ribbon the methods used in the present study might, therefore, not be able to detect very small differences in distribution. In the University of Goettingen a new method of microscopy was developed called one-step-nanoscale expansion (ONE) microscopy, which with the help of

the axial expansion of the specimen and a fluorescence fluctuation analysis is able to detect even single proteins, because of the great resolution it provides (Shaib et al., 2023). With a method like this and a resolution this high in the future there could be even more exact evaluations made concerning the distribution of the two RIBEYE Domains on the synaptic ribbon and further conclusions could be made regarding the structure of the synaptic ribbon.

Despite the findings of the last years, including those in the present study, it is still unclear how exactly RIBEYE builds the structure of the synaptic ribbon and more research is necessary. The present study did prove that the working model, showing the RIBEYE A-Domain as a structural domain building the synaptic ribbon at or around the core and the RIBEYE B-Domain interacting with the presynaptic environment on the surface of the ribbon, cannot ubiquitously be true. But what could the structure of the synaptic ribbon be?

Like described above RIBEYE is built by two individual subunits, the proline-rich RIBEYE A-domain that is unique to the protein and the RIBEYE B-Domain that is nearly identical to the transcriptional regulator CtPB2 except for the first 20 amino-terminal amino acids. CtBp2 is known to assemble into tetrameric structures, which is promoted by NADH. It is assumed that the RIBEYE B-Domain assembles in the same way because N-truncated versions of CtBP2 that lack 30 amino acids from CtBP2 also form tetramers (Bellesis et al, 2018, Nichols et al., 2021, Shankwar et al., 2022). The A-Domain on the other hand is rich in the amino acid proline. Proline is known for inhibiting the conformation of alpha-helixes and beta-sheets in a protein´s secondary structure, and tends to be located on the borders of them. The proline residues, due to their cyclic structure, introduce rigid angles into the secondary structure of the protein and are often found in turns of the protein backbone (Morgan and Rubenstein, 2013, Melnikov et al., 2016). Considering these structural properties and the findings in the present study, the assembly of the RIBEYE protein could look like what can be seen in Figure 31. Assuming that the RIBEYE B-Domains assemble into tetrameric structures to form the ribbon, the proline-rich A-Domain would curve to the outside of these tetramers connecting with other RIBEYE A-Domains. In this way the distribution of the RIBEYE domains along the width of the ribbon, would be very similar, just like in the results of the present study.

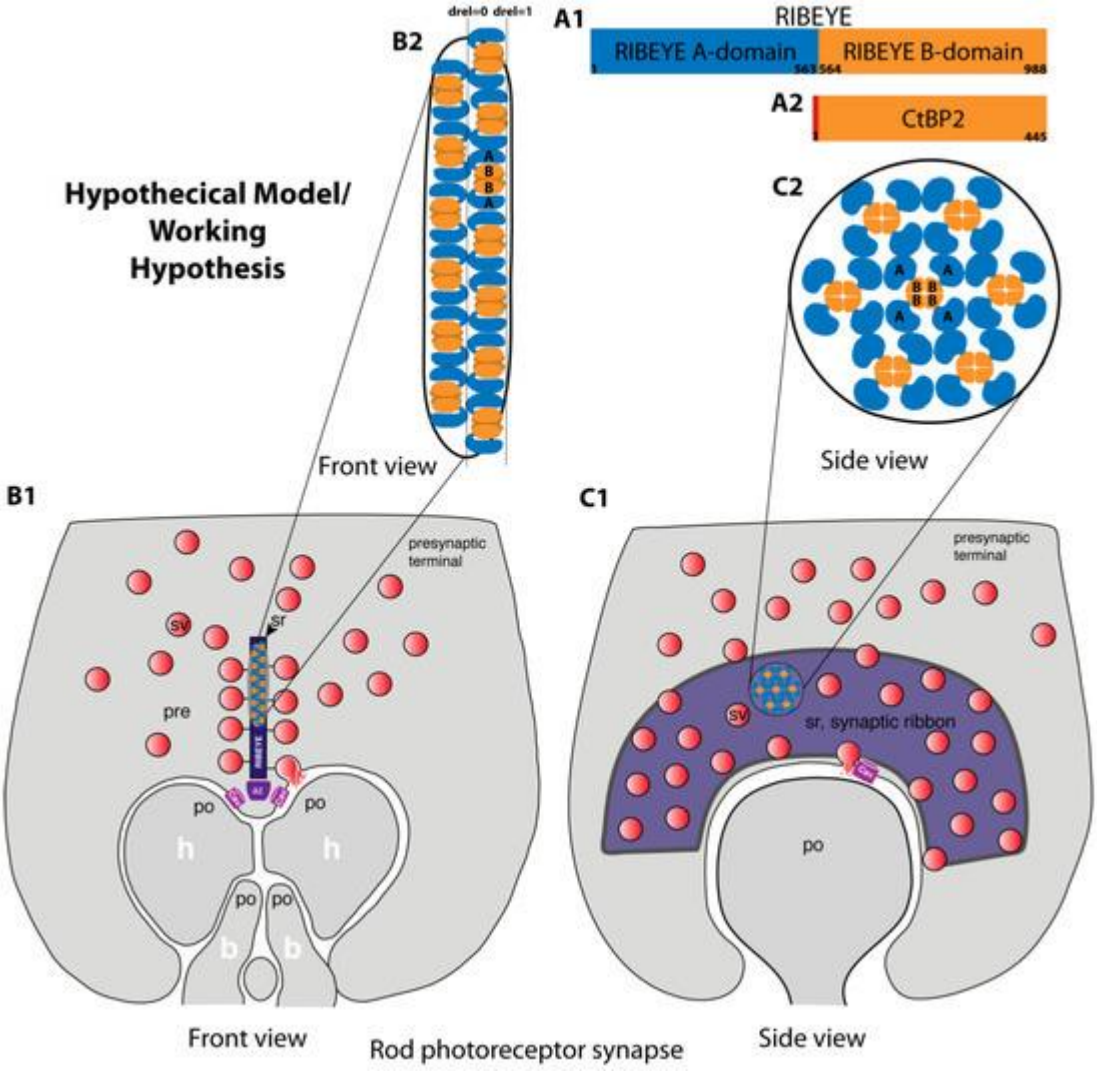

Figure 31: Refined Working hypothesis of the assembly of the synaptic ribbon (A1) Schematic representation of RIBEYE and its A-domain here depicted in blue and C-terminal B-domain shown in orange. Numbers below the proteins indicate amino acid numbers within the respective proteins. (B-C) Schematic drawing of a rod photoreceptor ribbon synapse shown from front view (B1) and side view (C1). (B2, C2) Magnification of the indicated regions of the synaptic ribbon schematically magnified to show the proposed assembly model. Abbreviations: $d_{rel=0}$ = midline of the synaptic ribbon, $d_{rel=1}$ = outer border of the synaptic ribbon, sr = synaptic ribbon, sv = synaptic vesicle, Cav = voltage-gated calcium channels, az = active zone, pre = presynaptic terminal, po = postsynaptic dendrites, h = horizontal cell dendrite, b = bipolar cell dendrite. Papadopoulos et al., 2024.

5 References

1. Adly, M. A., Spiwoks-Becker, I., Vollrath, L. (1999). Ultrastructural Changes of Photoreceptor Synaptic Ribbons in Relation to Time of Day and Illumination. *Investigative Ophthalmology & Visual Science 40(10), 21165-72.*
2. Alpadi, K., Magupalli, V. G., Käppel, S., Köblitz, L., Schwarz, K., Seigel, G. M., Sung, C. H., Schmitz, F. (2008). RIBEYE recruits Munc119, a mammalian ortholog of the Caenorhabditis elegans protein unc119, to synaptic ribbons of photoreceptor synapses. *Journal of Biological Chemistry*, *283*(39), 26461–26467. https://doi.org/10.1074/jbc.M801625200
3. Balkema, G. W., Cusick, K., Nguyen, T.-H. (2001). Diurnal variation in synaptic ribbon length and visual threshold. *Visual Neuroscience*, *18*(5), 789–797.
4. Chinnadurai, G. (2009). The transcriptional corepressor CtBP: A foe of multiple tumor suppressors. *Cancer Research*, *69*(3), 731–734. https://doi.org/10.1158/0008-5472.CAN-08-3349
5. Dembla, E., Dembla, M., Maxeiner, S., Schmitz, F. (2020). Synaptic ribbons foster active zone stability and illumination-dependent active zone enrichment of RIM2 and Cav1.4 in photoreceptor synapses. *Scientific Reports*, *10*(1), 5957. https://doi.org/10.1038/s41598-020-62734-0
6. Dembla, M., Kesharwani, A., Natarajan, S., Fecher-Trost, C., Fairless, R., Williams, S. K., Flockerzi, V., Diem, R., Schwarz, K., Schmitz, F. (2018). Early auto-immune targeting of photoreceptor ribbon synapses in mouse models of multiple sclerosis. *EMBO Molecular Medicine*, *10*(11). https://doi.org/10.15252/emmm.201808926
7. Dembla, M., Wahl, S., Katiyar, R., Schmitz, F. (2014). ArfGAP3 is a component of the photoreceptor synaptic ribbon complex and forms an NAD(H)-regulated, Redox-

sensitive complex with RIBEYE that is important for endocytosis. *Journal of Neuroscience*, *34*(15), 5245–5260. https://doi.org/10.1523/JNEUROSCI.3837-13.2014

8. Edelhoch, H. (1967). Spectroscopic Determination of Tryptophan and Tyrosine in Proteins. *Biochemistry*, *6*(7), 1948–1954.
9. Faulk, W. P., Taylor, G. M. (1971). An immunocolloid method for the electron microscope. *Immunochemistry*, *8*, 1081–1083.
10. Heidelberger, R., Thoreson, W. B., Witkovsky, P. (2005). Synaptic transmission at retinal ribbon synapses. *Progress in Retinal and Eye Research*, *24*(6), 682–720.
11. Hoon, M., Okawa, H., Della Santina, L., Wong, R. O. L. (2014). Functional architecture of the retina: Development and disease. *Progress in Retinal and Eye Research*, *42*, 44–84. https://doi.org/10.1016/j.preteyeres.2014.06.003
12. Hopsu, V. K., Arstila, A. U. (1964). An Apparent Somato-Somatic Synaptic Structure in the Pineal Gland of the Rat. *Experimental Cell Research*, *37*, 484–487.
13. Horisberger, M., Clerc, M.-F. (1985). Labelling of colloidal gold with protein A A quantitative study. In *Histochemistry* 82,219. Springer-Verlag.
14. Ichinose, T., Habib, S. (2022). On and off signaling pathways in the retina and the visual system. *Frontiers in Ophthalmology*, *2:989002*. https://doi.org/10.3389/fopht.2022.989002
15. Jeon, C.-J., Strettoi, E., Masland, R. H. (1998). *The Major Cell Populations of the Mouse Retina*. *J. Neurosci. 18(21), 8936-8946*
16. Kesharwani, A., Schwarz, K., Dembla, E., Dembla, M., Schmitz, F. (2021). Early changes in exo-and endocytosis in the EAE mouse model of multiple sclerosis correlate with decreased synaptic ribbon size and reduced ribbon-associated vesicle pools in rod photoreceptor synapses. *International Journal of Molecular Sciences*, *22(19), 10789.* https://doi.org/10.3390/ijms221910789

17. Laemmli, U. K. (1970). Cleavage of Structural Proteins during the Assembly of the Head of Bacteriophage T4. *Nature, 227(5259), 680-5. doi: 10.1038/227680a0.*

18. Lagnado, L., Gomis, A., Job, C. (1996). Continuous Vesicle Cycling in the Synaptic Terminal of Retinal Bipolar Cells. In *Neuron 17, 957–967*

19. Magupalli, V. G., Schwarz, K., Alpadi, K., Natarajan, S., Seigel, G. M., Schmitz, F. (2008). Multiple RIBEYE-RIBEYE interactions create a dynamic scaffold for the formation of synaptic ribbons. *Journal of Neuroscience*, *28*(32), 7954–7967.

20. Masland, R. H. (2001). The fundamental plan of the retina. *Nature Neuroscience*, *4,* 877–886.

21. Matthews, G., Fuchs, P. (2010). The diverse roles of ribbon synapses in sensory neurotransmission. *Nature Reviews Neuroscience*, *11*, 812–822.

22. Maxeiner, S., Luo, F., Tan, A., Schmitz, F., Südhof, T. C. (2016). How to make a synaptic ribbon: RIBEYE deletion abolishes ribbons in retinal synapses and disrupts neurotransmitter release. *EMBO J, 35, 1098–1114.*

23. McCartney M., Dickson D. (1985). Photoreceptor synaptic ribbons: Three-dimensional shape, orientation and diurnal (non) variation. Experimental Eye Research, 41 (3), 313-321.

24. Müller, F., Kaupp, U. B. (1998). Signaltransduktion in Sehzellen. *Naturwissenschaften Review Articles*, *85*, 49–61.

25. Nakajima Y., Iwakabe H., Akazawa C., Nawa H., Shigemoto R., Mizuno N., Nakanishi S. (1993). Molecular characterization of a novel retinal metabotropic glutamate receptor mGluR6 with a high agonist selectivity for L-2-amino-4-phosphonobutyrate. Journal of Biological Chemistry, 268 (16), 11868-11873.

26. Newman, E., Reichenbach, A. (1996). The Müller cell: A functional element of the retina. *Trends in Neurosciences*, *19*(8), 307–312.

27. Papadopoulos, S., Tinschert, R., Papadopoulos, I., Gerloff, X., Schmitz, F. (2024). Analytical Post-Embedding Immunogold–Electron Microscopy with Direct Gold-Labelled Monoclonal Primary Antibodies against RIBEYE A- and B-Domain Suggests a Refined Model of Synaptic Ribbon Assembly. Int. J. Mol. Sci. 25 (13), 7443.
28. Rao-Mirotznik, R., Harkins, A. B., Buchsbaum, G., Sterling, P. (1995). Mammalian rod terminal: Architecture of a binary synapse. Neuron, 14 (3), 561-569.
29. Schmitz, F. (2009). The making of synaptic ribbons: How they are built and what they do. *Neuroscientist, 15*(6), 611–624.
30. Schmitz, F., Königstorfer, A., Südhof, T. C. (2000). RIBEYE, a Component of Synaptic Ribbons: A Protein's Journey through Evolution Provides Insight into Synaptic Ribbon Function *Neuron 28, 857–872.*
31. Shaib, A.H., Chouaib, A. A., Chowdhury, R., Mihaylov, D., Zhang, C., Imani, V., Georgiev, S.V., Mougios, N., Monga, M., Reshetniak, S., Mimoso, T., Chen, H., Fatehbasharzad, P., Crzan, D., Saal, K., Alawar, N., Eilts J., Kang, J., Alvarez, L., Trenkwalder, C., Mollenhauer, B., Outeiro, T. F., Köster, S., Preobraschenski, J., Becherer, U, Moser, T., Boyden, E.S., Aricescu, A.R., Sauer, M., Opazo, F., Rizzoli, S. O. (2023). *Visualizing proteins by expansion microscopy Cluster of Excellence 'Multiscale Bioimaging: From Molecular Machines to Networks of Excitable Cells'*. https://doi.org/10.1101/2022.08.03.502284
32. Shankhwar, S., Schwarz, K., Katiyar, R., Jung, M., Maxeiner, S., Südhof, T. C., Schmitz, F. (2022). RIBEYE B-Domain Is Essential for RIBEYE A-Domain Stability and Assembly of Synaptic Ribbons. *Frontiers in Molecular Neuroscience*, *15*: 838311 https://doi.org/10.3389/fnmol.2022.838311
33. Silverthorn, D. U. (2015). *Human Physiology: An integrated Approach*. Pearson.

34. Singh A., Hamedinger D., Hoda J. C., Gebhart M., Koschak A., Romanin C., Striessnig J (2006). C-terminal modulator controls Ca2+-dependent gating of Ca(v)1.4 L-type Ca2+ channels. Nat Neurosci.9(9), 1108-16. https://doi.org/10.1038/nn1751

35. Slot, J. W., Geuze, H. J. (1985). A new method of preparing gold probes for multiple-labeling cytochemistry. *Journal of Cell Biology*, *38*(1), 87–93.

36. Smith, C. A., Sjöstrand, F. S. (1961). Structure of the nerve endings on the external hair cells of the guinea pig cochlea as studied by serial sections. *Journal of Ultrastructure Research*, *5*(6), 523–556.

37. Spiwoks-Becker, I., Glas, M., Lasarzik, I., Vollrath, L. (2004). Mouse photoreceptor synaptic ribbons lose and regain material in response to illumination changes. *European Journal of Neuroscience*, *19*(6), 1559–1571. https://doi.org/10.1111/j.1460-9568.2004.03198.x

38. Sterling, P., Matthews, G. (2005). Structure and function of ribbon synapses. *Synaptic Connectivity Series*, *28*(1), 20–29.

39. Tan, Y. H., Liu, M., Nolting, B., Go, J. G., Gervay-Hague, J., Liu, G. Y. (2008). A nanoengineering approach for investigation and regulation of protein immobilization. *ACS Nano*, *2*(11), 2374–2384.

40. Thoreson, W. B. (2007). Kinetics of synaptic transmission at ribbon synapses of rods and cones. *Molecular Neurobiology*, *36*(3), 205–223. https://doi.org/10.1007/s12035-007-0019-9

41. Tom Dieck, S., Altrock, W. D., Kessels, M. M., Qualmann, B., Regus, H., Brauner, D., Fejtova, A., Bracko, O., Gundelfinger, E. D., Brandstätter. Johann H. (2005). Molecular dissection of the photoreceptor ribbon synapse. *Journal of Cell Biology*, *168*(5), 825–836.

42. VaithianathanT., Henry D., Akmentin W., Matthews G. (2016). Nanoscale dynamics of synaptic vesicle trafficking and fusion at the presynaptic active zone. eLife 5, 13245.

43. Vaithianathan, T., Matthews, G. (2014) Visualizing synaptic vesicle turnover and pool refilling driven by calcium nanodomains at presynaptic active zones of ribbon synapses. Proc. Natl. Acad. Sci. U.S.A. 111, 8655–8660

44. Venkatesan, J. K., Natarajan, S., Schwarz, K., Mayer, S. I., Alpadi, K., Magupalli, V. G., Sung, C. H., Schmitz, F. (2010). Nicotinamide adenine dinucleotide-dependent binding of the neuronal Ca 2+ sensor protein GCAP2 to photoreceptor synaptic ribbons. *Journal of Neuroscience*, *30*(19), 6559–6576. https://doi.org/10.1523/JNEUROSCI.3701-09.2010

45. Wagner, H.-J. (1997). Presynaptic bodies ('ribbons'): From ultrastructural observations to molecular perspectives. *Cell & Tissue Reserach*, *287*, 435–446.

46. Watanabe, T., Raff, M. C. (1988). Retinal astrocytes are immigrants from the optic nerve. *Letters to Nature*, *332*, 834–837.

47. Yang, S., Zhou, J., Li, D. (2021). Functions and Diseases of the Retinal Pigment Epithelium. *Frontiers in Pharmacology*, *12*. https://doi.org/10.3389/fphar.2021.727870

48. Zenisek, D. (2008). Vesicle association and exocytosis at ribbon and extraribbon sites in retinal bipolar cell presynaptic terminals. Proc. Natl. Acad. Sci. U.S.A. 105, 4922–4927.

6 List of Abbreviations

aka	also known as
ap	affinity purified
APS	ammonium persulfate
Au-particles	gold particles
bc	bipolar cell
BSA	bovine serum albumin
°C	degree Celsius
cGMP	cyclic guanosinemonophosphate
c-terminal	carboxy terminal
CtBP	C-terminal binding protein
CTR	control (negative control)
Cys	cystein
d1	distance 1
d2	distance 2
d_i	relative distance of gold particles located inside of the marked area of the synaptic ribbon
d_o	relative distance of gold particles located outside of the marked area of the synaptic ribbon
d_{rel}	relative distance
d_{rel0}	number of gold particles at relative distance 0
d/dd_{rel}	first derivative of function $f(d_{rel})$
ddH_2O	double-destilled water
et al.	et alii (and others)
$f(d_{rel})$	function in dependence of d_{rel}
Fab portion	Fragment antigen-binding region

Fc portion	fragment crystallisable portion
G6F4/G2D9	grid labelled with 6F4/2D9
GDP/GTP	guanosine di-/triphosphate
hc	horizontal cell
hr/hrs	hour/hours
i.e.	id est
IgG	immunoglobulin G
INL	inner nuclear layer
IPL	inner plexiform layer
kDa	kiloDalton
L-type calcium channel	low-voltage activating calcium channel
lim	limit of a sequence (mathematics)
LR-Gold	
M	molar
M opsin	middle-wavelength opsin
m1/m2/m3	mouse 1/mouse 2/ mouse 3
mg	milligram
min	minutes
ml	mililiter
mm	milimeter
mM	milimol
µg	microgram
µl	microliter
µm	micrometer
NADH	nicotinamide adenine dinucleotide hydrogen
ng	nanogram
nm	nanometer

ONL	outer nuclear layer
OPL	outer plexiform layer
p	probability value
PAGE	polyacrylamide gel electrophoresis
PBS	phosphate buffer saline
PDE	phosphodiesterase
PFA	paraformaldehyde
pH	potential hydrogen
Na-terminal	amino terminal
R	set of real numbers (mathematics)
rpm	rounds per minute
SDS	sodium dodecyl sulfate
S opsin	short-wavelength opsin
SV	synaptic vesicles
TEMED	tetramethyl ethylenediamine
TEM	transmission electron microscopy
tot	total
UV light	ultraviolet light

7 List of Figures and Tables

8 Publication

As part of the dissertation the following manuscript was publicised in the International Journal of Molecular Sciences:

Papadopoulos, S., Tinschert, R., Papadopoulos, I., Gerloff, X., Schmitz, F. (2024). Analytical Post-Embedding Immunogold–Electron Microscopy with Direct Gold-Labelled Monoclonal Primary Antibodies against RIBEYE A- and B-Domain Suggests a Refined Model of Synaptic Ribbon Assembly. Int. J. Mol. Sci. 25 (13), 7443.